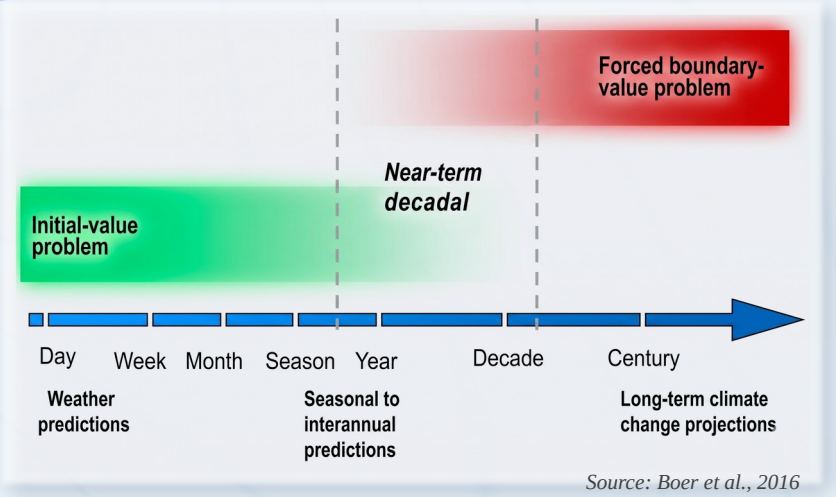
ISSN 0252-1075
Contribution from IITM
Research Report No. RR-150
ESSO/IITM/CVP/SR/03(2026)/212

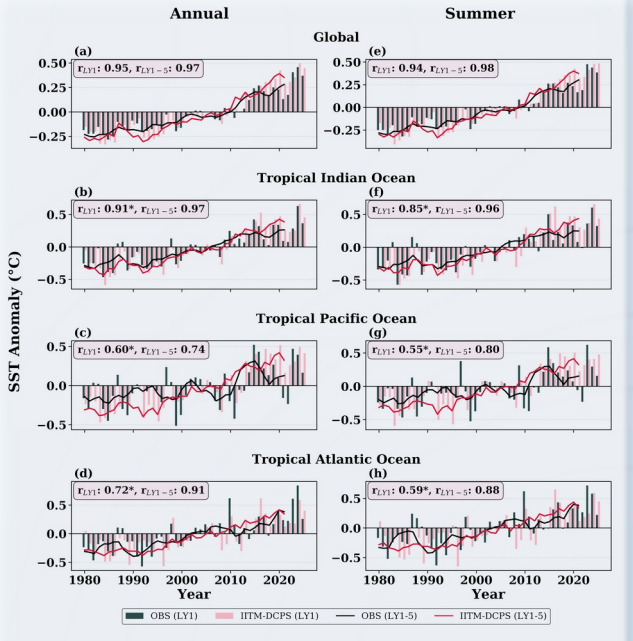
Evaluation/Hindcast Skill Assessment of the IITM Decadal Climate Prediction System for 1979-2024

Rosimitha Panda, C. Gnanaseelan, P.V. Rajesh, Saikat Pramanik, Darshana Patekar, J.S. Deepa, Amit Kumar Sharma, Rahul Pai, Amol Vibhute, A.G. Prajeesh, Anant Parekh, Jasti Chowdary, Suryakanti Dutta

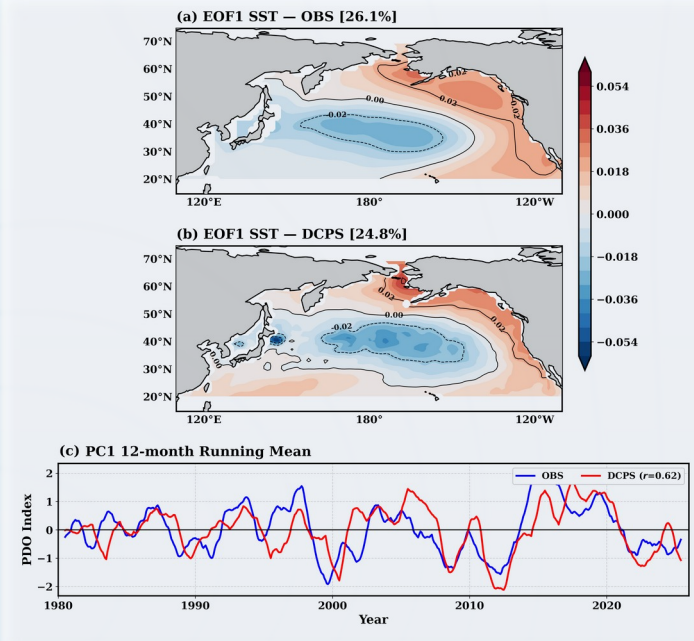


Source: Boer et al., 2016

SST Skill for the Globe and Tropical Basins



Pacific Decadal Oscillation (PDO)



Indian Institute of Tropical Meteorology (IITM)
Ministry of Earth Sciences (MoES)
PUNE-411008, INDIA
https://www.tropmet.res.in/

ISSN 0252-1075
Contribution from IITM
Research Report No. RR-150
ESSO/IITM/CVP /SR/03(2026)/212

Evaluation/Hindcast Skill Assessment of the IITM Decadal Climate Prediction System for 1979-2024

Rosimitha Panda[1], C. Gnanaseelan[1,*], P.V. Rajesh[1], Saikat Pramanik[1], Darshana Patekar[1], J.S. Deepa[1], Amit Kumar Sharma[1], Rahul Pai[1,2], Amol Vibhute[1], A.G. Prajeesh[1,3], Anant Parekh[1], Jasti Chowdary[1], Suryakanti Dutta[4]

[1] Climate Variability and Prediction, Indian Institute of Tropical Meteorology, Ministry of Earth Sciences, Pune 411 008 India.
[2]New York University, Abu Dhabi, UAE.
[3]King Abdullah University of Science & Technology, Saudi Arabia.
[4]National Centre for Medium Range Weather Forecasting, Noida.

***Corresponding Author:**
Dr. C. Gnanaseelan
Scientist G and Project Director
Climate Variability and Prediction (CVP)
Indian Institute of Tropical Meteorology,
Dr. Homi Bhabha Road, Pashan, Pune-411 008, India.
E-mail: seelan@tropmet.res.in
Phone: +91 -(0)20-259 04 271

Indian Institute of Tropical Meteorology (IITM)
Ministry of Earth Sciences (MoES)
PUNE-411008, INDIA
https://www.tropmet.res.in/

DOCUMENT CONTROL SHEET

Ministry of Earth Sciences (MoES)
Indian Institute of Tropical Meteorology (IITM)

ESSO Document Number
ESSO/IITM/CVP /SR/03(2026)/212

Title of the Report
Evaluation/Hindcast Skill Assessment of the IITM Decadal Climate Prediction System for 1979-2024

Authors
Rosimitha Panda, C. Gnanaseelan*, P.V. Rajesh, Saikat Pramanik, Darshana Patekar, J.S. Deepa, Amit Kumar Sharma, Rahul Pai, Amol Vibhute, A.G. Prajeesh, Anant Parekh, Jasti Chowdary, Suryakanti Dutta

Reviewers
Dr Abhisek Chatterjee,
[Scientist 'E', Indian National Centre for Ocean Information Services (INCOIS), Hyderabad]
Dr. Ramesh K. Vellore
[Scientist ‘F’, Indian Institute of Tropical Meteorology, Pune]

Type of Document
Scientific Report

Number of pages and figures
45, 21

Number of references
84

Keywords
Decadal Climate Prediction, Hindcast, Indian Monsoon, Teleconnection.

Security classification
Open

Distribution
Unrestricted

Date of Publication
October 2026

Abstract:

Initialized decadal climate prediction systems provide an important framework for predicting near-term climate variability by combining externally forced climate signals with internally generated variability arising from ocean-atmosphere interactions. The present study assesses the hindcast skill of the IITM Decadal Climate Prediction System (IITM-DCPS), which contributes to CMIP6 DCPP-A and consists of 10-member ensembles of 10-year predictions initialized each November from 1979 to 2024. The prediction skill of key climate variables, including Sea Surface Temperature (SST), near-surface air temperature (SAT), and precipitation (PR), is assessed using anomaly correlation coefficients (ACC) for Lead Year 1 (LY1) and multi-year averages of Lead Years 1-5 (LY1-5). The results show high prediction skill for global SST and SAT in both leads, with correlations exceeding 0.9 across most ocean basins along with several continental regions. Precipitation skill is relatively lower and spatially variable, with better predictability mainly over tropical regions and global northern hemisphere. At global and basin scales, the system reproduces the observed temporal evolution of SST variability, with skill highest over the tropical Indian Ocean ($r > 0.90$), followed by the tropical Atlantic and the tropical Pacific ($r \approx 0.55$-0.60), reflecting the dominance of the externally forced warming in the Indian Ocean against the stronger internal variability of the Pacific. The model well represents the El Niño Southern Oscillation (ENSO) variability and its teleconnections with the Indian summer monsoon at LY1, especially during the peak season. At LY1, the Interdecadal Pacific Oscillation (IPO)-related rainfall variability over the Indo-Western Pacific is captured well during the decay phase of El Nino events. Skill evaluation of major climate indices, including the Atlantic Multidecadal Oscillation (AMO), Pacific Decadal Oscillation (PDO), and IPO, indicates that the model represents important low-frequency oceanic variability contributing to decadal prediction skill. The leading mode of North Pacific SST variability in IITM-DCPS reproduces the observed PDO-like spatial pattern and shows improved agreement with observations at decadal timescales, with the PC1 correlation of 0.62, showing the model's ability to capture low-frequency climate variability. Strong prediction skill is also evident in Arctic sea ice concentration and sea level anomalies, with anomaly correlations exceeding 0.6 and 0.8, respectively as noted in several regions over Arctic and the tropical Indo-Pacific and Indian Ocean regions. Over the South Asian region, the system shows very good skill in predicting SASCOF rainfall in both LY1 and LY1-5, this highlights the potential of IITM-DCPS in skilfully predicting the South Asian rainfall years ahead. The regional rainfall predictability however decreases at longer lead times and is evident in the Indian Summer Monsoon Rainfall (ISMR). Despite regional biases and reduced precipitation skill at extended leads, IITM-DCPS demonstrates useful near-term prediction capability over South Asia, parts of India, and the surrounding Indian Ocean. Overall, the results suggest that IITM-DCPS provides reliable near-term climate predictions such as monsoon teleconnections, Indian Ocean SST and sea level etc. The large-

scale temperature variability and the leading climate modes are captured well, highlighting its potential for operational decadal prediction and climate risk assessment.

Summary:

This study evaluates the performance of the IITM Decadal Climate Prediction System (IITM-DCPS) in predicting near-term climate variability using initialized decadal hindcasts generated following the CMIP6 DCPP-A protocol. A 10-member ensemble of hindcasts initialized every November from 1979 to 2024 is analyzed to assess prediction skill for sea surface temperature (SST), surface air temperature (SAT), precipitation, sea level anomalies, sea ice concentration, and major climate variability indices.

The results indicate that IITM-DCPS exhibits high skill in predicting global SST variability, with relatively consistent performance across lead times, particularly over the tropical Indian Ocean, where the externally forced warming signal contributes substantially to predictability. In contrast, skill is comparatively lower over the eastern equatorial Pacific, including the Niño 3.4 region, reflecting the challenges associated with ENSO variability. SAT predictions also show substantial skill over both land and ocean, with improved performance in multi-year averages. The system captures major modes of climate variability, including ENSO, AMO, PDO, IPO, and Indian Ocean variability, highlighting the contribution of large-scale ocean-atmosphere interactions to decadal prediction skill. Sea level anomaly and Arctic sea ice predictions also indicate useful skill in representing large-scale oceanic and cryospheric variability.

Precipitation predictability remains more challenging than temperature predictability because of strong internal atmospheric variability. Nevertheless, IITM-DCPS shows useful skill in predicting Indian summer monsoon rainfall, particularly over northwestern and peninsular India, while skill remains weak or negative over the Central Monsoon Zone (CMZ) and eastern India. The relatively better skill over northwestern and peninsular India may be associated with large-scale circulation features, including the low-level jet and orographic influences along the Western Ghats.

Overall, the evaluation highlights the potential of IITM-DCPS for predicting large-scale climate variability on decadal timescales and supporting regional climate outlooks, including SASCOF activities. However, improving rainfall prediction over central and eastern India remains a key challenge. Future development should focus on improving the representation of monsoon synoptic systems and low-level circulation, strengthening land-atmosphere interactions, incorporating interactive aerosol processes, and reducing ocean mean-state biases to improve IOD prediction skill. These improvements are expected to further enhance the predictive capability of IITM-DCPS, particularly for Indian monsoon rainfall.

Contents

1. Introduction 1

2. Model, Datasets used and Methodology 3

2.1 Model 3
2.2 Hindcast experiment 3
2.3 Datasets 4
2.4 Methodology 5

3. Results 6

3.1 Global Prediction Skill of IITM-DCPS 6
3.1.1 Sea Surface Temperature 7
3.1.2 Near-Surface Air Temperature 8
3.1.3 Precipitation 9
3.2 Temporal evolution of Global and Regional SST 10
3.2.1 Climate Indices 11
3.3 Skill of Indian Summer Monsoon Rainfall in Decadal Hindcasts 13
3.4 Lead-Lag Relationship between ENSO and ISMR 15
3.5 Regional skill assessment 16
3.6 Indo-Pacific Teleconnections 17
3.7 Evaluation of the Pacific Decadal Oscillation (PDO) 20
3.8 Prediction Skill of Sea Level Variability 20
3.9 Prediction Skill of SIC over Arctic 21

4. Summary and Conclusions 21

Acknowledgements 24
References 24
Figures 31

1. Introduction

Decadal climate predictions provide an essential framework for evaluating and comparing climate model simulations with observations, thereby advancing our understanding of the climate system's intrinsic predictability and the dominant mechanisms controlling variability on interannual to decadal timescales (Boer et al., 2015; Balakrishnan et al., 2019; Merryfield et al., 2020) which is crucial for improving near-term climate prediction. Understanding these variations is fundamental not only for climate advancement but also for developing reliable climate services that can inform adaptation strategies and risk management decisions (Meehl et al., 2014). The predictable climate variability at these timescales is driven by a complex interplay of external radiative forcings and internal variability of the system. External radiative forcings include natural factors such as solar and volcanic activity, as well as anthropogenic influences such as greenhouse gas emissions, aerosol concentrations, and land-use changes, which collectively alter the Earth's energy balance (Smith et al., 2020). Thus, unlike centennial climate projections that focus primarily on response to changing external forcings, decadal prediction uses an approach that includes a combination of both an initialization with observed conditions and external forcing (Towler et al., 2018).

Annual to multidecadal variations of sea surface temperatures (SSTs), such as the El Niño Southern Oscillation (ENSO), Indian Ocean Dipole (IOD), Atlantic Multidecadal Oscillation (AMO), Pacific Decadal Oscillation (PDO), the Interdecadal Pacific oscillation (IPO) (Power et al. 1999) and decadal TIOSST or Indian Ocean Basin Mode (IOBM) (e.g., Vibhute et al. 2020; Halder et al. 2022) provide the sources of potential skill for prediction on interannual to decadal time scale (Meehl et al. 2014). Many previous studies analyzed the prediction skill of decadal variability of climate over midlatitudes and extratropical regions. For example, Simpson et al. (2019) showed by using Community Earth System Model-Decadal Prediction Large Ensemble (CESM-DPLE) that AMO prediction skill may be used to predict decadal prediction skill of precipitation over Europe via the association between Atlantic multidecadal variability and the North Atlantic eddy-driven jet. Athanasiadis et al. (2020) found that the CESM-DPLE exhibits remarkable decadal prediction skill in reproducing variations of wintertime blocking frequency over the North Atlantic and of the North Atlantic Oscillation (NAO) with maximum skill in the lead year range 1 to 8. Further, Marcheggiani et al. (2023) expanded this work by demonstrating that the winter NAO is predictable over the lead year range of 2-9 using component A of the Decadal Climate Prediction Project (DCPP) models from Coupled Model Intercomparison Project Phase-6 (CMIP6; Boer et al. 2016). They further showed that this predictable NAO can be used to quantify the skill in capturing the location and speed of the North Atlantic eddy-driven jet.

Recent advances have revealed promising skill in decadal temperature predictions over large regions of the globe, with evidence that this skill extends beyond what can be explained by external forcing alone (Xie et al., 2015). However, precipitation predictions remain more challenging, with lower skill compared to temperature, although progress is being made through improved understanding of the mechanisms linking oceanic variability to regional precipitation patterns (Smith et al., 2019). Prediction capabilities in different regions require specialized attention to local climate drivers and mechanisms. For regions heavily dependent on monsoon rainfall, such as the Indian subcontinent, reliable decadal predictions could revolutionize water resource management, agricultural planning, and disaster preparedness (Konda et al., 2023). The tropical Indo-Pacific region, which includes the Indian monsoon domain, presents unique challenges and opportunities for decadal prediction (Dong et al., 2024). This region experiences complex interactions between the Pacific and Indian Oceans, including phenomena such as the Indo-Pacific Warm Pool expansion, Walker Circulation changes, and monsoon variability. Understanding and predicting these regional phenomena requires models that accurately represent both global climate dynamics and teleconnections specific to the Indo-Pacific domain (Darshana et al., 2022; Dong et al., 2024; Tokinaga et al., 2012). Utilizing a multi-model ensemble approach, which incorporates predictions from various models and multiple runs from each, helps to minimize the impact of errors and biases specific to individual models and provides a more reliable estimate of future climate variability. Thus, even if some models have already examined decadal prediction for a specific region or variable, additional models contribute to a broader sampling of possible outcomes, increased robustness, and accelerated model improvement, all of which are essential for making more accurate and actionable climate forecasts (Smith et al., 2019; Carmo-Costa et al., 2025). To contribute to international multi-model decadal prediction initiatives and to build indigenous near-term climate prediction capability, the Indian Institute of Tropical Meteorology (IITM) developed the Decadal Climate Prediction System version 1 (IITM-DCPS), the first decadal prediction system developed for India (Rajesh et al., 2026). This system contributes to the DCPP under CMIP6 and directly supports the World Meteorological Organization's (WMO) Global Annual to Decadal Climate Update initiatives. However, a comprehensive evaluation of IITM-DCPS prediction skill across different climate variables, lead times, spatial scales, and major modes of climate variability, prediction capabilities and limitations is yet to be explored. The main objective of this study is to provide a comprehensive evaluation of the IITM-DCPS hindcast skill for global and regional (South Asia) climate on annual-to-decadal timescales. The prediction skill of key climate variables, including sea surface temperature (SST), near-surface air temperature (SAT), precipitation (PR), sea level anomalies (SLA), and Arctic sea ice concentration (SIC) is assessed, using hindcasts spanning 1979-2024. Further, this study evaluates the model's ability to represent the spatial and temporal characteristics of major modes of climate variability, including ENSO, PDO,

IPO, and AMO, and examines the ENSO-monsoon teleconnections. The analysis provides insights into the sources of predictability, the dependence of prediction skill on region and lead time, and the physical processes associated with the system. These findings highlight the strengths and limitations of IITM-DCPS and demonstrate its potential as a reliable framework for operational decadal climate prediction and climate services, particularly over South Asia and the broader Indo-Pacific region.

2. Model, Datasets used and Methodology

2.1 Model

In this study, we used the Earth System Model IITM-DCPS version 1 (here after IITM-DCPS) for the Decadal Climate Prediction. This model has contributed successfully to the CMIP6 for the DCPP of WMO Lead Center for preparing the Global Annual to Decadal Climate Update. The atmospheric component of the IITM-DCPS is based on the National Centers for Environmental Prediction (NCEP) Global Forecast System (GFS) model with T126 spectral resolution (~1°) and 64 sigma-pressure hybrid levels up to 0.2 hPa, using the simplified Arakawa-Schubert convection scheme with cumulus momentum mixing. It uses the Noah land surface model (LSM) version 2.7.1, which includes a single-layer snowpack, vegetation, and underlying soil layers. The Ocean component is Modular Ocean Model version 4p1 (MOM4p1) with a horizontal resolution of 0.5° in the zonal and 0.25° in the meridional direction, which gradually coarsens beyond 30°S and 30°N, with 40 vertical levels in which 27 levels are concentrated in the upper 400 meters, allowing for better representation of upper ocean processes. The sea ice component is the Sea Ice Simulator version 1 (SIS), a coupled model described by Delworth et al. (2006), which represents sea ice as a three-layer system with five thickness categories. Interactive biogeochemistry is included through the Tracers of Phytoplankton with Allometric Zooplankton (TOPAZ) module, allowing the model to simulate ocean and sea-ice dynamics, thermodynamics, and tracer changes influenced by physical and biogeochemical processes. Additional details about the model are described in Rajesh et al., (2026).

2.2 Hindcast experiment

Our decadal prediction system, IITM-DCPS, follows the CMIP6 DCPP-A protocol (Boer et al., 2016) and therefore consists of 10-member ensembles of 10-year-long predictions, initialized from observed states and forced with CMIP6 historical conditions up to the present, followed by the SSP2-4.5 scenario. These hindcasts were generated using atmospheric initial conditions provided by the National Centre for Medium Range Weather Forecasting (NCMRWF). Operational atmospheric analyses at NCMRWF are generated using the Grid point Statistical Interpolation (GSI)-based Hybrid Four-Dimensional Ensemble Variational (4D-EnVar) data assimilation system, which blends flow-dependent ensemble covariances with static background error covariances in 6-hourly cycles

assimilating conventional and satellite observations (Wang and Lei, 2014; Lorenc et al., 2015; Prasad et al., 2016). For this decadal prediction system, a 10-member ensemble of atmospheric initial conditions was generated using the Perturbed Ensemble (PE) approach. The perturbations are generated from the difference between the 48-h and 24-h GFS forecasts, both valid at the same verification time. These 48-24 h forecast differences are appropriately scaled and centered to obtain zero-mean perturbations across the ensemble. The resulting perturbations are then added to and subtracted from the central analysis to generate the ten-member ensembles of atmospheric initial conditions.

The ocean initial conditions are indigenously prepared following the approach of Bilbao et al. (2021), using a Newtonian relaxation (nudging) technique to assimilate three-dimensional Ocean Reanalysis System 5 (ORAS5) temperature and salinity fields. The relaxation timescale increases with depth, set approximately to 10 days at 1000m, 100 days at 3000m, and 330 days at 5000m. This subsurface nudging is applied globally, except within the equatorial band (3°S-3°N), to avoid the development of artificial vertical velocities. The surface atmospheric fields are constrained to ERA5 reanalysis during the assimilation phase to ensure consistency with observed surface conditions. The model initialization was performed every year on 1st November from 1979 to 2024. A time-varying monthly mean green vegetation fraction dataset from the Land-Use Harmonization (LUH2, Hurtt et al.,2020) dataset, along with monthly varying stratospheric aerosols (volcanic forcing) and other external forcings such as greenhouse gases, ozone, and solar radiation, was used in the IITM-DCPS decadal hindcasts following the CMIP6 DCPP protocol. The schematic of the Hindcast strategy is provided in Figure 1.

2.3 Datasets

The datasets used in this study include both observational and reanalysis estimates to assess the skill of the IITM-DCPS hindcasts for key variables, namely SST, SAT, and precipitation, which were further used to calculate climate indices over both global and regional domains. The latest version of the Extended Reconstructed Sea Surface Temperature dataset, version 5 (ERSSTv5), with a spatial resolution of 2° × 2°, is used for SST evaluation (Huang et al., 2017). Precipitation skill is assessed using the Global Precipitation Climatology Project (GPCP) version 2 dataset (Adler et al., 2003). SAT is validated against the ERA5 reanalysis dataset with a horizontal resolution of 0.25° (Hersbach et al., 2020). The ORAS5 global ocean reanalysis fields have been used for evaluating SIC and sea level variability (Balmaseda et al., 2019). The model initialised in November of every year from 1979 to 2024, runs for the span of next 10 years from each initialised year (called lead year 1, lead year 2,…, lead year 10). For example, a model that was initiated in November 1980, runs for the period from November 1980 to December 1990. The forecast/prediction of 1981 is considered as the lead year 1,

1982 is considered as the lead year 2 etc., for the model initialised in November 1980. The same approach is followed for all the initialised years starting from November 1979 to November 2024. Therefore, the lead year 1 (LY1) prediction/forecast ranges from the year 1980 to 2025 and likewise the lead year 1-5 (LY1-5) prediction represents the average of the first five forecast years following each initialization and ranges from 1980 to 2020. Before the analysis, all observational and hindcast data are re-gridded from their original spatial resolutions to a common resolution of 1° × 1°.

2.4 Methodology

Initialized predictions drift away from the observed state and relax towards the model's own climatology as the integration proceeds, so the mean state of the hindcast is a function of forecast lead time. This drift is corrected using a lead-time-dependent climatology approach, following standard DCPP practice (Hawkins et al.,2014; Boer et al., 2016). For each variable, season and forecast year, the climatology is the mean over all initializations of that same forecast year, evaluated over the common 1991-2020 reference period. This climatology is subtracted from the corresponding forecast to obtain the model anomalies. The same period used as the reference baseline for the observed anomalies, ensuring consistency between model and observed fields. This 30-year baseline is adopted in accordance with the current standard climatological normal defined by the WMO (WMO, 2021) and adheres to the CMIP6: DCPP-A (Boer et al., 2016) verification protocols. Using this standardized baseline aligns with operational decadal prediction updates, providing a robust baseline that reflects the satellite-era observation density and recent climate warming trends. The skill of decadal predictions is evaluated using deterministic verification metrics, primarily the Pearson anomaly correlation coefficient (ACC) (Ho et al., 2013). The ACC represents the temporal correlation between forecast and observed anomalies and measures the ability of the model to reproduce observed variability. The ACC ranges between −1 and +1, where +1 indicates perfect agreement, 0 indicates no linear relationship, and −1 represents perfect anti-correlation. Further, climate variability is assessed using several large-scale climate indices derived from SST anomalies. The ENSO is represented by the Niño 3.4 index, calculated as the area-averaged SST anomaly over the east-central equatorial Pacific region (5°N-5°S, 170°W-120°W). The AMO index is computed as the basin-averaged SST anomaly over the North Atlantic region (0°-60°N, 80°W-0°). The Atlantic Niño index is defined as the SST anomaly averaged over the equatorial Atlantic region (3°S-3°N, 20°W-0°). The IPO index is calculated as the difference between SST anomalies averaged over the central equatorial Pacific (10°S-10°N, 170°E-90°W) and the mean SST anomalies over the Northwest Pacific (25°N-45°N, 140°E-145°W) and Southwest Pacific (50°S-15°S, 150°E-160°W), following Henley et al. (2015). The PDO index is derived from SST anomalies over the North Pacific domain (120°E-120°W, 20°-60°N; Mantua et al., 1997). The IOD index is calculated following the Dipole Mode Index (DMI)

definition as the difference between western and eastern equatorial Indian Ocean SST anomalies. The western box (IOD_W) is defined over the region (10°S-10°N, 50°E-70°E), while the eastern box (IOD_E) is defined over (10°S-0°, 90°E-110°E). A five-year low-pass filtering effect is inherently included in the lead-year averaged forecasts (LY1-5). Therefore, no additional external temporal smoothing or low-pass filtering is applied to the indices. In addition to Global scale SST variability, basin-scale variability is examined over the Tropical Indian Ocean (TIO; 30°S-30°N, 40°E-110°E), Tropical Pacific Ocean (TPO; 20°S-20°N, 120°E-80°W), and Tropical Atlantic Ocean (TAO; 20°S-20°N, 70°W-0°), where the indices are calculated as area-averaged SST anomalies over the respective domains. To investigate large-scale teleconnections, statistical techniques including singular value decomposition (SVD) analysis (Wallace et al., 1992; Deser and Timlin, 1997), along with correlation and regression analyses, are employed to examine coupled variability between different oceanic and atmospheric fields. The PDO index was computed separately for the IITM-DCPS hindcast ensemble mean and the observational SST dataset following the standard Mantua-Zhang method (Mantua et al.,1999., Zhang et al., 1997). Monthly SST fields were first remapped to a common 1° × 1° regular grid using bilinear interpolation and spatially subset to the North Pacific domain (110°E-250°E, 20°N-70°N). A linear trend was removed at each grid point to eliminate long-term drift, and the global-mean SST anomaly was subtracted at each time step to isolate internally generated decadal variability from the externally forced warming signal. EOF analysis was then applied to the processed North Pacific SST field, and the PDO index was defined as the standardised PC1 time series of the leading EOF. This procedure was applied identically to both the hindcast and observational datasets to ensure a consistent and directly comparable evaluation.

3. Results

3.1 Global Prediction Skill of IITM-DCPS

Assessing the prediction skill of key climate variables is essential for evaluating the performance of initialized decadal climate prediction systems. Among these variables, SST, SAT, and PR represent fundamental components of the climate system, governing ocean-atmosphere interactions, surface energy balance, and the global hydrological cycle. Accurate prediction of these variables is crucial for understanding and forecasting large-scale climate variability and its regional impacts. In initialized decadal prediction systems, the predictability of climate largely arises from slowly varying components of the climate system, particularly the ocean, which provides long-term memory that can influence atmospheric conditions over multiple years (Meehl et al., 2014; Boer et al., 2016). Therefore, evaluating the skill of these key variables provides a comprehensive assessment of the model's ability to represent both oceanic persistence and atmospheric responses.

In this study, the prediction skill of SST, SAT, and PR is assessed using the ACC between the ensemble mean of hindcasts and observational datasets. The spatial distribution of ACC is examined globally for the first lead year (LY1) as well as the multi-year average of Lead Years 1-5 (LY1-5). The analysis is performed for the annual mean and for the seasons, including January-February (JF), March-May (MAM), June-September (JJAS), and October-December (OND). These seasonal analyses allow assessment of the model's ability to capture variability across different phases of the annual cycle, including periods characterized by strong ocean-atmosphere coupling and seasonal climate transitions. The following sections present the global spatial patterns of ACC for SST, SAT, and PR, respectively, for different seasons and lead times, highlighting regions of strong prediction skill as well as areas where the model exhibits limited predictability.

3.1.1 Sea Surface Temperature

The global spatial patterns of the ACC for SST show strong prediction skill across both LY1 and LY1-5 shown in figure 2, the model maintains high correlation values ($r > 0.9$) across the vast majority of the global oceans, with the most pronounced skill concentrated in the tropical Pacific and Indian Ocean basins. These regions of high ACC are consistently marked by stippling, confirming that the prediction skill is statistically significant at the 95% confidence level. By contrast, skill is comparatively lower over the eastern equatorial Pacific, including the Niño3.4 region, a pattern broadly consistent with other decadal prediction systems, which similarly show greater skill in the North Atlantic, western Pacific, and Indian Oceans than elsewhere (Meehl et al., 2014). The physical basis of this skill differs between basins. Over the TIO the predictable signal is dominated by the externally forced response to increasing greenhouse gas concentrations, the ratio of internally generated to externally forced variance is the lowest there of all tropical basins, which makes this the region of highest decadal SST skill worldwide and makes that skill only weakly dependent on lead time (Guemas et al., 2013). Over the equatorial Pacific, by contrast, the LY1 skill originates mainly from the initialized ocean state and from the persistence of the upper-ocean heat content that precedes ENSO events, so it decays more rapidly as the memory of the initial conditions is lost and as the diversity of ENSO events, which models represent imperfectly, becomes the limiting factor (Chowdary et al., 2025).

A comparative analysis of the temporal scales reveals that the LY1-5 attains marginally higher global mean correlations than LY1. While LY1 shows strong annual and seasonal performance, with global correlation values ranging from 0.89 to 0.95, the LY1-5 panels exhibit a notable enhancement in overall skill, reaching a peak of 0.98 during the JJAS season. The high skill in the North Atlantic and Pacific sectors further suggests the model's capacity to represent long-term fluctuations such as the AMO and the IPO. However, given the limited sample size underlying these correlations, such

differences between LY1 and LY1-5 are within the range of sampling uncertainty and should be interpreted as broadly comparable skill rather than a significant improvement. This caveat applies to all LY1-5 results that follow, as the overlapping five-year means are strongly autocorrelated and their effective sample size is correspondingly reduced.

Seasonal variability in prediction skill remains relatively stable, although subtle fluctuations are present. The highest global correlations are observed during MAM and JJAS seasons which may reflect the model's ability to maintain signal persistence following the boreal spring predictability barrier (Webster & Yang, 1992). In contrast, a slight reduction in global skill is observed during OND for LY1 (0.89), possibly associated with the transitional nature of tropical sea surface temperature anomalies during boreal autumn. Despite these minor seasonal variations, correlations above 0.9 and widespread statistical significance across both LY1 and LY1-5 indicate a consistent level of prediction skill, comparable to that reported in state-of-the-art models participating in the CMIP6 -DCPP.

3.1.2 Near-Surface Air Temperature

The global spatial distribution of the ACC for SAT (Figure 3) indicates that prediction skill is not limited to the oceans but also extends over land regions. Consistent with the strong thermodynamic coupling between the ocean and atmosphere, the large-scale oceanic ACC patterns are reflected in the overlying atmospheric temperature field (Kushnir et al., 2019). As a result, the SAT field exhibits substantial predictability over several continental regions. High correlation values ($r > 0.9$) are particularly evident over northern Eurasia, the African continent, and tropical South America across all seasons. The widespread statistically significant correlations over these regions suggest that the combined influence of ocean initialization and external radiative forcing contributes to improved near-surface temperature prediction at the 95% confidence level.

A comparison between the LY1 and the LY1-5 highlights a substantial reduction in atmospheric noise with increasing lead time averaging. In the LY1 panels, regional heterogeneity is more pronounced over mid-latitude landmasses especially during the JF and OND seasons (Figure 3b, e). This spatial variability primarily arises from the dominance of internal atmospheric dynamics. at these lead times. During these seasons, stochastic circulation modes such as the NAO and Arctic Oscillation (AO) introduce substantial interannual variability, often obscuring the predictable climate signal at shorter lead times (Kushnir et al., 2019). Land-surface feedback add a further, seasonally distinct source of noise: during the warm season, nonlinear soil moisture-temperature interactions over transitional climate regions can amplify localized variability, where soil-moisture deficits enhance sensible heat fluxes and intensify regional warming anomalies, resulting in the fragmented ACC patterns observed in the LY1 panels (Seneviratne et al., 2010). However, in the LY1-5 average, these high-frequency fluctuations are effectively filtered, leading to high ACC values (0.96-0.98). This enhancement

suggests that the model is able to capture the forced response and low-frequency climate signals, such as the decadal warming trend, which are of greater relevance for long-term policy and adaptation planning (Smith et al., 2019; Yeager et al., 2018). Furthermore, the SAT results indicate a relatively stable predictability across seasons. These findings suggest that IITM-DCPS provides consistent near-term climate prediction skill over both global oceans and continental regions.

3.1.3 Precipitation

Compared to temperature fields, the global prediction skill for precipitation (Figure 4) shows considerably greater spatial heterogeneity and lower overall correlation values, reflecting the inherently high variability and stochastic nature of rainfall processes. The ACC for precipitation indicates that the highest skill is mainly confined to tropical ocean regions, particularly the central and eastern Pacific and parts of the Indian Ocean. These regions of statistically significant skill suggest that the model captures large-scale atmospheric responses to SST forcing, especially those associated with the ENSO, which is a major source of global precipitation predictability (Goddard et al., 2001; Smith et al., 2012).

Seasonal analysis shows that precipitation skill is relatively higher during boreal winter (JF) and spring (MAM) for LY1, with global mean correlations of about 0.31 and 0.45, respectively. These seasons generally coincide with the mature phase of dominant tropical climate modes. In contrast to temperature predictability, however, the transition from LY1 to the LY1–5 does not lead to a systematic improvement in precipitation skill. Although some regions, including high latitudes and parts of the tropical Atlantic, display more spatially coherent patterns in LY1-5, the global mean correlations decrease and become weak or slightly negative during JJAS and OND. This behaviour reflects the difficulty of predicting precipitation at multi-year timescales, as rainfall variability is strongly influenced by transient convective processes and internal atmospheric variability that can slower climate signals (Kirtman et al., 2013; Scaife et al., 2014).

The model also shows localized skill over several land regions, including the Maritime Continent, parts of northern Africa, and high-latitude Eurasia. The presence of statistically significant correlations in these areas indicates that the system captures aspects of land-atmosphere interactions and remote teleconnections originating from oceanic variability. Nevertheless, precipitation skill over continental regions remains spatially fragmented, consistent with the well-known signal-to-noise problem in decadal prediction, where meaningful regional predictability can coexist with relatively low global mean skill (Scaife and Smith, 2018; Smith et al., 2019). Overall, while precipitation predictability is weaker than temperature predictability, the persistence of significant tropical skill across lead times suggests that the system can still provide useful information on large-scale

variations in the global hydrological cycle.

The limited precipitation skill over land is not only a consequence of a low signal-to-noise ratio, it also reflects specific structural uncertainties of the coupled system. The simplified convection scheme governs how predicted SST anomalies are converted into diabatic heating, and its excessive sensitivity to local instability produces noisy, overly ENSO-responsive rainfall that masks the initial signal (Dwivedi et al., 2026). Soil moisture-precipitation and evapotranspiration feedbacks in the land-surface model further modulate the persistence of continental rainfall anomalies and are a recognized source of inter-model spread in decadal rainfall skill (Seneviratne et al., 2010), while the prescribed rather than interactive treatment of historical anthropogenic aerosols, despite contributing substantially to the multi-decadal rainfall signal over South and East Asia introduces additional uncertainty through aerosol forcing and aerosol-cloud interactions (Forster, 2020; Smith et al., 2019). Together with the intrinsic unpredictability of transient convective systems, these structural uncertainties explain why precipitation skill remains fragmented over land even where the underlying SST and large-scale circulation are predicted well.

3.2 Temporal evolution of Global and Regional SST

Figure 5 presents the temporal evolution of SST anomalies over the global ocean and three tropical basins: the TIO, TPO, and TAO for both annual mean and JJAS season, comparing observations with IITM-DCPS hindcasts at LY1 and LY1-5. At the global scale, the model reproduces the observed long-term SST variability closely, with anomaly correlations exceeding 0.94 across both lead configurations and seasons. The high agreement primarily reflects the dominance of large-scale externally forced warming signals, which contribute substantially to global SST variability. The slightly higher correlations for LY1-5 indicate the expected effect of temporal averaging, whereby short-term internal variability is reduced and lower-frequency variability becomes more evident, consistent with characteristics of initialized decadal prediction systems (Smith et al., 2007; Boer et al., 2016).

Over the TIO, relatively high skill is maintained, particularly in the annual mean, with correlations above 0.90. This suggests that the model captures the basin-wide SST evolution and associated large-scale variability reasonably well. A modest reduction in skill during JJAS likely reflects the influence of monsoon-related air–sea interactions, regional upwelling processes, and intraseasonal variability, which introduce additional complexity during the summer monsoon season (Saji et al., 1999; Swapna et al., 2015). The stability of this skill across lead times is a robust feature of decadal prediction systems and reflects the dominance of the externally forced warming over internal variability in this basin, together with the long thermal memory of the TIO mixed layer, the potential predictability of

TIO SST in CMIP6 DCPP models remains essentially flat from LY1 to LY10, in contrast to the equatorial Pacific (Guemas et al., 2013; Chowdary et al., 2025).

The TPO exhibits comparatively lower correlations for LY1 in both annual and JJAS timescales, with values around 0.55-0.60. Rather than indicating a complete lack of predictability, this reduction reflects the strong internally generated variability and nonlinear ocean-atmosphere coupling that characterize ENSO dynamics. Small phase shifts or amplitude differences in ENSO events can substantially reduce correlation metrics even when the overall variability and associated large-scale impacts are reasonably represented. Consistent with this interpretation, improvements seen in the LY1-5 averages suggest that multi-year averaging reduces high-frequency variability and enhances the representation of lower-frequency Pacific variability. This behavior does not limit the model from capturing ENSO teleconnections, which depend more on large-scale circulation responses than on exact SST phase agreement. This behaviour is in agreement with the potential-predictability analysis carried out on the CMIP6 DCPP hindcasts, since the skill associated with equatorial Pacific SST drops from around 0.9 at LY1 to about 0.6 by LY10, whereas that of the TIO is almost independent of lead time. Further, the remaining difference between the potential and actual skill in this basin is due to the variety of ENSO events, since the coupled models represent the longitudinal position and intensity of these events imperfectly, and also because of biases in the simulated ocean mixing which influence the recharge and discharge of equatorial heat content (Richter, 2015; Chowdary et al., 2025).

The TAO shows moderate skill, with correlations varying by season and lead time. The model reproduces the general warming trend and portions of interannual variability, although skill remains lower than in the TIO. This may be related to the comparatively weaker and more regionally sensitive modes of Atlantic variability, including Atlantic Niño processes and cross-equatorial SST gradients, which remain challenging for many coupled models (Richter et al., 2014). As in other basins, multi-year averaging improves agreement with observations, indicating better representation of lower-frequency variability than short-term fluctuations.

Overall, the results suggest that IITM-DCPS shows higher consistency at larger spatial scales and for slowly varying components of SST variability, while skill decreases in regions dominated by strong internal variability and complex coupled dynamics. The systematic improvement from LY1 to LY1-5 across basins highlights the role of temporal averaging in enhancing decadal predictability, consistent with the broader understanding that decadal prediction systems tend to represent large-scale, low-frequency climate variability more robustly than regional or high-frequency variations.

3.2.1 Climate Indices

To assess the ability of IITM-DCPS to capture large-scale climate variability, dominant oceanic climate indices are analyzed as indicators of basin-scale predictability. Figure 6 to 8 shows the

timeseries and associated ACC skill of various dominant oceanic indices across Annual, JJAS and their respective peak season timescales for the IITM-DCPS hindcasts at LY1 and LY1-5, along with observations. The IITM-DCPS demonstrates significant prediction skill across a diverse suite of climate modes, including AMO, PDO, IPO, ENSO (Niño 3.4), Atlantic Niño (AT-Nino), eastern and western IOD (IOD-E and IOD-W). The model shows high fidelity in reproducing the long-term evolution of these indices, particularly the pronounced positive phases of the AMO and PDO, as well as the observed negative phase of the IPO since the late 1990s. For the AMO and PDO, ACC values reach exceptionally high levels ($r \geq 0.92$ for LY1-5), indicating that the prediction system effectively captures the low-frequency thermal memory of the Atlantic and Pacific basins. The high skill of these low-frequency indices comes from two main sources. The AMO and PDO/IPO reflect slowly varying subsurface ocean heat content, directly constrained by ORAS5-based ocean initialization and persisting over several years. Both indices also include a significant externally forced component linked to greenhouse gas and aerosol forcing (Boer et al., 2016; Smith et al., 2019; Carmo-Costa et al., 2025). In contrast, ENSO skill at LY1 is mainly an initial-value problem, as initialized Pacific upper-ocean heat content persists through the first forecast year (Chowdary et al., 2025). Notably, the model exhibits skill in predicting ENSO during its peak season (DJF Niño 3.4), with ACC values reaching 0.40 for LY1 (Figure 8), confirming the model's ability to represent the mature phase of the ENSO. While the individual eastern and western boxes of the IOD (IOD-E and IOD-W) display significant prediction skill, the combined IOD index shows comparatively lower ACC values. In IITM-DCPS, the prediction skill is higher over the western equatorial Indian Ocean (IOD-W) than over the eastern equatorial Indian Ocean (IOD-E). This asymmetric prediction skill is consistent with the findings of Paul et al. (2026), with higher predictability over the western equatorial Indian Ocean compared to the eastern equatorial Indian Ocean in DCPP-CMIP6 decadal hindcast models. The higher predictability over the western equatorial Indian Ocean is associated with stronger ocean-atmosphere coupling and greater oceanic memory, whereas the eastern equatorial Indian Ocean has relatively lower ocean memory and greater atmospheric variability. Since the IOD index represents the zonal SST gradient between the western and eastern equatorial Indian Ocean, the relatively lower prediction skill over the eastern pole can contribute to the reduced skill of the combined IOD index, even when the western pole is predicted relatively well (Paul et al., 2026). The IOD also depends on coupled ocean-atmosphere processes involving equatorial wind anomalies, thermocline variations, and upwelling-related SST changes, particularly over the eastern Indian Ocean (Saji et al., 1999; Li et al., 2003). Therefore, improving IOD prediction may require better representation and initialization of the ocean subsurface state, thermocline variability, and air–sea coupling, particularly over the eastern equatorial Indian Ocean. In Summary, its consistent representation of key multidecadal modes

and peak-season ENSO variability, highlights its effectiveness as an advanced prediction framework for near-term decadal climate prediction.

3.3 Skill of Indian Summer Monsoon Rainfall in Decadal Hindcasts

The predictability of ISMR during the JJAS season remains a major challenge in climate prediction due to the complex interactions between ocean-atmosphere processes, land-surface feedback, and internal atmospheric variability. Given the monsoon's central role in India's agriculture and water resources, evaluating the performance of decadal prediction systems in representing the spatial variability of monsoon precipitation is therefore essential.

The spatial distribution of anomaly correlations for JJAS precipitation between IITM-DCPS hindcasts and observations is shown for LY1 and the multi-year mean of LY1-5 (Figure 9). During LY1 (Figure 9a), the model exhibits positive correlations across large parts of India, indicating that the system captures a significant fraction of the observed interannual variability of monsoon rainfall during the first forecast year. Strong positive correlations are particularly evident over northwestern India and parts of western India, suggesting that the model is able to represent large-scale circulation features that influence rainfall variability in these regions. Moderate positive correlations are also observed over peninsular India, indicating reasonable skill in simulating regional precipitation variability associated with monsoon circulation and its interaction with the Western Ghats orography and land-surface interactions. However, relatively weak or negative correlations appear over parts of central India, which is one of the core monsoon rainfall (Core Monsoon Zone; CMZ) regions may be related to the challenges in representing lows and depressions, the associated synoptic scale variability, mesoscale convection, land-atmosphere feedback, and intraseasonal variability that strongly influence rainfall variability in this region This reduced skill over the CMZ is a consequence of the dominant role of synoptic-scale variability in determining the seasonal rainfall total. Monsoon low-pressure systems and depressions contribute an estimated 45%-55% of seasonal rainfall over central India and account for most of its year-to-year variability, yet their number, genesis location and tracks vary from year to year in a largely chaotic manner (Yoon and chen.,2005). Coupled climate models are known to systematically underrepresent the frequency and intensity of these synoptic disturbances (Goswami et al., 2014; Srivastava et al., 2017). Applying the sub-seasonal band decomposition of Yashas et al. (2026), we found that the synoptic (2-5 d) band in IITM-DCPS accounts for 8.0%-9.5% of total JJAS daily rainfall variance, against 10.9% in observations. The primary limitation in correlation skill over the CMZ therefore arises from the chaotic interannual timing of these systems, rather than their frequency or intensity. Although the model's underrepresentation of their frequency and intensity affects the simulated rainfall amount and variance, these amplitude differences alone do not necessarily determine the correlation skill, which

depends more strongly on the agreement in the temporal evolution and phase of the rainfall anomalies. Mesoscale organization of convection, soil moisture-rainfall feedback and intraseasonal active-break variability act on the same seasonal totals and could further reduce the predictable fraction.

For the LY1-5 (Figure 9b), the spatial structure of rainfall prediction skill changes considerably. While moderate positive correlations persist over parts of northwestern India and southern peninsular India, indicating that some predictable signals remain at longer lead times, the skill decreases across several regions of central and eastern India, where negative correlations emerge, reaching −0.5 to −0.6 over Odisha, the eastern Gangetic plain and Himalayan region. This reduction in skill with increasing lead time reflects the gradual weakening of initialization effects and the increasing influence of chaotic internal atmospheric variability. Lower skill over the Himalayan and northern northeast regions may also reflect the difficulty of representing complex orographic effects and localized precipitation processes at the relatively coarse resolution of global coupled models. Regions that maintain some prediction skill are likely influenced by slowly varying boundary conditions such as SST variability in the TIO and TPO, which are known to modulate monsoon rainfall variability on interannual to decadal timescales (Kirtman et al., 2013; Smith et al., 2019)

Taken together, the results indicate that the IITM-DCPS captures the spatial variability of JJAS precipitation with useful skill during the first forecast year. However, the prediction skill decreases at longer lead times, particularly over central monsoon regions, where the chaotic interannual timing of synoptic-scale low-pressure systems limits the attainable correlation, while their underrepresentation in the model acts on the simulated rainfall amount and its variance. In contrast, prediction skill is better over northwestern and peninsular India, reflecting the model's capacity to simulate large-scale circulation and orographic rainfall linked to the low-level jet and the Western Ghats. Nevertheless, the persistence of positive correlations in certain regions indicate that large-scale ocean-atmosphere interactions, particularly SST variability in the tropical Indian and Pacific Oceans, provide a source of predictability for the ISM at multi-year timescales. Improving the representation of monsoon dynamics, convection, and land-atmosphere coupling may further enhance the predictive skill of decadal forecasts over the Indian region.

Figure 10 represents the annual cycle of rainfall over the Indian domain (72°E-98°E, 10°N-32°N) provides a critical benchmark for the model's ability to simulate the seasonal evolution of the ISM. IITM-DCPS follows the climatological monthly rainfall distribution closely for both LY1 and LY1-5, capturing the sharp transition from the dry pre-monsoon months to the monsoon onset in June, with rainfall peaking in July broadly consistent with the observed climatology. A detailed examination of the monsoon months (JJAS) reveals that while the DCPS accurately follows the seasonal trajectory, it exhibits a slight dry bias during the peak rainfall period in July and August. In July, where observed

rainfall reaches approximately 10 mm/day, the DCPS forecasts for both LY1 and LY1-5 under-predict the magnitude by roughly 1 mm/day. This dry bias is a common characteristic of coupled climate models and is attributable primarily to the underrepresentation of synoptic-scale monsoon low-pressure systems, which deliver a large part of the July-August rainfall over central India and which are too few and too weak in coupled climate models (Goswami et al., 2014; Srivastava et al., 2017). The bias is compounded by the convective parameterization, which precipitates moisture prematurely over the equatorial Indian Ocean and thereby weakens the moisture supply to the monsoon trough (Goswami et al., 2014). This is consistent with an equatorward displacement of the monsoon low-level jet in the model's simulated circulation (**not shown**). Despite this slight underestimation, the phasing of the monsoon withdrawal in September and October is well captured by the DCPS, almost perfectly coinciding with the observations.

Interestingly, the annual cycles for LY1 and LY1-5 are nearly identical within the model, indicating that the mean seasonal climatology is consistently represented across different lead times. The close alignment between the red (LY1) and blue (LY1-5) dashed lines indicates that the model's internal climatology does not suffer from significant drift in the transition from seasonal to decadal scales. Such stability in the simulated annual cycle provides confidence that predicted anomalies evolve relative to a realistic and stable seasonal background (Boer et al., 2016; Smith et al., 2019). Maintaining this level of seasonal accuracy over the Indian subcontinent suggests some potential relevance of IITM-DCPS for hydrological and agricultural planning applications.

3.4 Lead-Lag Relationship between ENSO and ISMR

The lead-lag correlation between all-India JJAS rainfall of forecast year 1 with monthly Niño 3.4 SST anomalies of forecast years 1 and 2 (Figure 11) is used to assess the model's ability to represent the temporal evolution of the ENSO-monsoon teleconnection. In observations (black line), the correlation is weakly positive during the pre-monsoon months of LY1, it is followed by a transition to a significant negative relationship during the monsoon season, with the correlation reaching approximately −0.60 during July-August. IITM-DCPS (red line) also captures the transition to a negative relationship and reproduces the strong inverse association during JJAS, with correlations reaching approximately −0.70 during June-August. However, unlike observations, the model develops a negative relationship during the pre-monsoon months of LY1, indicating an earlier onset of the ENSO-ISMR teleconnection. Similar differences in the seasonal timing of the ENSO-monsoon relationship have been reported in coupled climate models. Annamalai et al. (2007) showed that the ENSO-monsoon relationship exhibits substantial differences in its seasonal evolution across IPCC AR4 models, including differences in the timing of the transition between positive and negative rainfall-ENSO correlations. The boreal spring transition is a critical period in the ENSO cycle, during

which changes in the background state and the seasonally varying ENSO growth rate influence ENSO evolution and phase locking and contribute to the spring predictability barrier (Torrence and Webster, 1998; Levine and McPhaden, 2015). The earlier development of the negative relationship in IITM-DCPS may therefore reflect differences in the simulated seasonal evolution of ENSO and its teleconnection with the Indian summer monsoon. Following the monsoon season, the negative correlation weakens in both observations and IITM-DCPS, although the weakening occurs more rapidly in the model. The stronger negative correlation during JJAS indicates a stronger statistical coupling between Niño3.4 SST anomalies and ISMR in IITM-DCPS than in observations. Overall, IITM-DCPS captures the dominant inverse ENSO-ISMR relationship during the monsoon season and its subsequent weakening, while differences remain in the timing of the onset, magnitude, and persistence of the teleconnection.

3.5 Regional skill assessment

Following the evaluation of large-scale climate variability and ISM characteristics, the model performance is further examined over the South Asian region (60^{o}E-100^{o}E,0^{o}-40^{o}N) and Extended Indian Monsoon Region (EIMR) (70^{o}E-110^{o}E, 10^{o}N-30^{o}N) domains. Evaluating these regions are important, as temperature and rainfall variability over South Asia directly influence agriculture and water resources.

From the figures 12 and 14 it is observed that the results for SAT indicate consistent performance at the regional scale. Over the South Asian region (Figure 12), the ACC values remain high, ranging from 0.90 to 0.98. Similar behaviour is observed over the EIMR region (Figure 14), where ACC values range from 0.81 to 0.88 for LY1 and increase to about 0.97 for the LY1-5. In both regions, the model captures the observed warming trend, reflected in the shift from negative anomalies before 2000 to persistent positive anomalies afterward. The relatively narrow ensemble spread suggests stable and consistent temperature evolution across ensemble members. This high skill largely reflects the dominance of the externally forced warming signal, which is predictable at long lead times and becomes clearer under multi-year averaging.

Precipitation prediction (Figures 13 and 15) remains inherently challenging due to the strong influence of regional processes. Despite this complexity, the system shows useful skill over both regions. Over the South Asian domain, ACC values range between 0.48 and 0.76, so that between about a quarter and a half of the observed interannual variance is reproduced. Over the EIMR region, skill is evident for both annual and JJAS rainfall, with further improvement seen in the LY1-5. Although differences in individual years are present, the forecasts capture several observed wet and dry phases. Compared to typical performance reported in many CMIP6 models, the precipitation skill

obtained here is relatively strong, suggesting that the initialized prediction system effectively captures large-scale drivers influencing South Asian rainfall variability. The residual differences between the predicted and observed rainfall series over these domains arise mainly from three sources: the equatorward displacement of the low-level jet (not shown) and which leads to deficit in moisture transport into the monsoon trough; the excessive sensitivity of the parameterized convection to ENSO forcing, which amplifies the modelled rainfall response to Pacific SST anomalies (Section 3.6); and the prescribed, non-interactive treatment of anthropogenic aerosols, which contribute a large part of the multi-decadal rainfall variation over South Asia and whose forcing remains among the most uncertain in CMIP6 models (Forster, 2020; Smith et al., 2019).

3.6 Indo-Pacific Teleconnections

ENSO is a key driver of climate variability in the Indo-Pacific region and is closely tied to the annual cycle. Typically, ENSO starts developing during summer, reaches its peak in winter, and then declines rapidly by April of the following year. ENSO is closely phase-locked to the seasonal cycle, with events typically reaching their peak during the boreal winter (e.g., Rasmusson and Carpenter 1982).

Figure 16 provides a comprehensive assessment of the skill of the IITM-DCPS coupled climate model in predicting ENSO evolution in comparison to observations (OBS), focusing on 1-year lead forecasts. Figure 16a presents lead-lag correlation coefficients between the boreal winter (December-February, D(0)JF(1)) Niño 3.4 index and the monthly Niño 3.4 SST index for the period 1981–2024. The observed Niño 3.4 autocorrelation illustrates the typical ENSO life cycle, in which event begin to develop in late spring or summer of Year(0), peak during boreal winter toward the end of the year and dissipate by the following spring of Year(+1). The IITM-DCPS is able to capture the overall ENSO evolution. However, the correlation magnitudes are slightly weaker as compared to OBS. In particular, the simulated ENSO peak (zero-lag correlation) is shifted toward the late winter, followed by more abrupt decline in the subsequent summer relative to OBS.

Figure 16b shows the summer (JJAS) Niño 3.4 index, indicating the developing stage of ENSO during summer. The model has ability to track observed interannual variability (correlation = 0.4) indicates moderate skill, though several years show significant discrepancies in amplitude or even sign, illustrating typical challenges for models in capturing the onset of ENSO events or distinguishing between El Niño and neutral conditions (eg. Barnston et al., 2012).

Figure 16c addresses the decaying ENSO summer (JJA of year(+1)) conditions, through the recently introduced Indo-western Pacific Ocean Capacitor (IPOC) mode (eg. Xie et al 2016) which is closely linked to the decay phase of ENSO in summer. During the ENSO decay phase, Basin wide SST in the TIO and low-level large-scale circulation over the western north Pacific (WNP) combine to form this leading mode over the Indo-Western Pacific (IWP). The IPOC represents the dominant pattern of

co-variability between interannual anomalies of WNP 850 hPa relative vorticity (0-60°N, 100-160°E) and TIO SST (20°S-25°N, 40°E-100°E) during summer (JJA) (plot not shown). A Singular Value Decomposition (SVD) analysis was conducted between WNP vorticity anomalies and TIO SST anomalies to extract the IPOC mode in both observations and the IITM-DCPS model (lead year 1). In observations, the first SVD mode explains 59% of the total covariance. Note that the leading principal component (PC1) defined here is the positive phase of IPOC index (Figure 16c) and is used to understand the post-El Niño impacts during summer (Similarly, negative IPOC mode is related to post-La Nina events). The model can predict the year-to-year variability of IPOC mode with significant correlation of 0.68 with OBS.

Figure 17 shows regression (correlation) of JJAS Niño 3.4 upon the global SST, SLP, and 850 hPa wind anomalies (precipitation) for the OBS and IITM-DCPS model with lead year 1. Warm SST anomalies associated with El Niño in the central-eastern equatorial Pacific are fairly predicted by model at lead year 1 but with more westward extension and weaker meridional expansion as compared to the OBS (Figures 17 a,c). The westward displacement of the warm SST anomaly, resulting in a Central Pacific-like ENSO signature, represents a well-known systematic bias in coupled models and has been associated with biases in the tropical Pacific mean state, including an excessively strong and westward-extended equatorial cold tongue and associated easterly wind stress biases (Jiang et al., 2021). These biases can shift the region of maximum air-sea coupling and associated deep convection westward and modify the zonal advective feedback, favouring a more westward or Central Pacific-like ENSO structure (Wang and Lin, 2023). In response to El Niño-related warming, anomalous low-level cyclonic circulations either side of the equator as a part of Matsuno-Gill pattern are apparent in both observation and model. However, the northern hemispheric cyclonic circulation is stronger and stretched towards WNP in the model. Strong easterly wind anomalies over ISM region, responsible for deficit monsoon, induced by El Niño over ISM region are well predicted by the model as seen in precipitation correlation (Figures 17 b,d). However, this strong negative ISM rainfall anomaly is coherent with the strong low-level anticyclonic circulation in model which is weak in OBS; indicating stronger circulation-convection feedback over ISM region in model than that of OBS. Additionally, as seen in the observations, the model accurately replicates the spatial distribution of SLP across the Indo-Pacific region except in the subtropical north Atlantic Ocean. Differences in the east-west orientation of SST anomalies between OBS and the model drive circulation differences over the TIO and the ISM region. In OBS, pronounced subsidence noticed over eastern TIO and Maritime continent as compared to ISM region. The model tends to overestimate and excessively spread the negative precipitation anomalies caused by El Niño-induced subsidence over the Indian region. Despite this, the model reasonably captures the impact of the developing phase of El Niño on the ISMR. This suggests that the IITM-DCPS is able to reasonably predict the

developing ENSO and its teleconnections with ISMR with lead year 1. The model's overestimation of the deficit in ISM rainfall associated with El Niño is attributed to the westward extension of El Niño-related warm SSTs and the Walker circulation, which differs from the observed patterns.

JJA SVD-PC1 (positive IPOC mode) is regressed upon SST, SLP and 850 hPa wind in observation and model and correlated with rainfall (Figure 18). Weak SST anomalies related to decaying El Niño over the equatorial Pacific region are noticed in OBS; while the model shows quick decay of El Niño compared to OBS. The key IPOC features ie. TIO basin wide SST warming and WNP anticyclone/positive SLP anomalies are well captured by the model similar to OBS with some differences. Notably, the model produces WNP anticyclone is stronger and broader; shifted north-eastward, with stronger easterlies relative to the observation (Figures 18 a,c) which is seen in SLP and 850 hPa wind anomalies. The pair of tropical anticyclonic and subtropical cyclonic circulations over WNP represent positive Pacific-Japan mode (Nitta 1986) that impacts East Asian monsoon (eg. Choi et al 2010) and south Asian monsoon (Srinivas et al 2018). Many previous studies suggest that the positive Pacific-Japan pattern is significantly related to the decay phase of El Niño (e.g., Sun et al. 2010; Xie et al. 2016).

Observations show that in response to the IPOC mode, a southwest-northeast dipole pattern emerges in precipitation over the ISM region when SVD-PC1 is correlated with JJA precipitation anomalies (Figure 18b). This pattern features a positive correlation over southern peninsular India and a negative correlation over the Indo-Gangetic Plain, which corresponds to the eastern part of the monsoon trough region (Chowdary et al., 2019; Darshana et al., 2020). Additionally, positive rainfall anomalies are observed over northeast India. The model at lead year 1 reasonably captures this dipole precipitation pattern (Figure 18d); however, the model overestimates the positive rainfall over southern peninsular India due to strong convergence of anomalous south-westerly winds from the Arabian Sea and easterly winds from the Bay of Bengal, which are weaker in the observations. The negative rainfall anomalies over the monsoon trough in observations result from the westward extension of the northwestern flank of the low-level WNP anticyclone; in the model, this extension is confined near the head of the Bay of Bengal, leading to weaker negative rainfall. The exaggerated anticyclonic circulation anomalies enhance subsidence and moisture divergence over the WNP, leading to excessive drying relative to observations. Consequently, while the model captures the IPOC-related rainfall response qualitatively, it overestimates the strength and spatial influence of the atmospheric teleconnection during the decaying phase of El Niño. The analysis reveals that the IITM-DCPS model at lead year 1 is reasonably capable of predicting IPOC-related rainfall patterns over the Indo-Western Pacific (IWP) region during the decay phase of El Niño.

3.7 Evaluation of the Pacific Decadal Oscillation (PDO)

The PDO is often described as a long-lived El Niño-like pattern of Pacific climate variability (Zhang et al. 1997). It represents the dominant mode of decadal-scale SST variability over the North Pacific and plays an important role in modulating large-scale climate variability and atmospheric teleconnections. The performance of IITM-DCPS in representing PDO variability was evaluated by comparing the leading Empirical Orthogonal Function (EOF1) of North Pacific SST anomalies and its associated Principal Component (PC1) time series with observations for the period 1980-2025. The observed EOF1 pattern, shown in Figure (19a), explains 26.1% of the total North Pacific SST variance and exhibits the characteristic 'horseshoe' shaped structure of the PDO, with negative anomalies concentrated in the central North Pacific and positive anomalies along the North American coast and the western Pacific regions. The IITM-DCPS successfully reproduces this dominant spatial pattern as seen in Figure (19b), explaining 24.8% of the total variance, which is in close agreement with the observations. The model captures the key structural features of the PDO, including central basin cooling and coastal warming signals. While minor differences in the amplitude and spatial extent of anomalies are evident, suggesting slight regional SST biases, the overall spatial agreement confirms that the model realistically represents large-scale decadal ocean variability over the North Pacific.

The PC1 time series comparison further highlights the model's temporal skill. At the monthly timescale, illustrated in Figure (19c), the model follows the observed phase transitions reasonably well with a correlation of 0.41. Although some phase mismatches and amplitude discrepancies occur during certain periods, the model's performance improves substantially when high-frequency seasonal noise is suppressed. As shown in Figure (19d), using a 12-month running mean increases the correlation to 0.62. This enhancement of skill at longer timescales is particularly evident during the major PDO regime shifts of the late 1990s and mid-2010s, confirming that the model correctly captures low-frequency phase transitions and multi-year persistence. Overall, these results suggest that the IITM-DCPS reproduces both the spatial structure and low-frequency temporal evolution of PDO-related SST variability with reasonable fidelity, establishing its credibility as a tool for long-range decadal climate prediction over the Pacific sector.

3.8 Prediction Skill of Sea Level Variability

Regional sea level variability superimposed on the long-term rise directly influences coastal flooding, storm-surge inundation, and saline intrusion along the densely populated Indian Ocean rim, making its multi-year prediction of considerable societal relevance. Sea level anomalies show ACC values above 0.8 across much of the tropical and subtropical Indo-Pacific at LY1, while predictive skill is largely maintained at LY1-5 (Figure 20). It is high in the TIO and the subtropical South Pacific but

lower in the eastern equatorial Pacific, reflecting the previously reported SST skill pattern. These findings align with recent CMIP6-based assessments, which indicate skilful decadal sea level prediction over the tropical Indo-Pacific at LY1, while higher skill persists at longer lead times mainly over the western Indian Ocean (Deepa and Gnanaseelan, 2024). Sea level variability in this region is mainly governed by steric changes linked to upper-ocean heat content and wind-driven thermocline adjustment, so the initialized three-dimensional temperature and salinity fields provide a direct source of predictability.

3.9 Prediction Skill of SIC over Arctic

The prediction skill of the IITM-DCPS hindcasts is further examined using cryospheric indicators. Arctic sea ice plays a crucial role in the climate system, influencing surface albedo, ocean-atmosphere heat exchange, and high-latitude atmospheric circulation. Reliable multi-year forecasts have become increasingly important for Arctic shipping and resource management. The ACC for SIC, assessed against ORAS5 (Figure 21), exceeds 0.6 in the Barents, Kara, and Chukchi Seas at LY1 and remains stable through LY1-5. In contrast, predictive skill is lowest in the central Arctic, sometimes even negative, likely due to differences in predictability sources: marginal ice zones are influenced by ocean heat transport and ocean initial conditions, whereas central Arctic variability is dominated by wind-driven ice motion that is not predictable at these lead times (Yeager et al., 2015; Guemas et al., 2016; Reifenberg and Goessling, 2022).

4. Summary and Conclusions

This study evaluates the performance of the IITM-DCPS in predicting near-term climate variability using initialized decadal hindcasts generated following the CMIP6 DCPP-A protocol. A set of 10-member ensemble hindcasts initialized every November from 1979 to 2024 is analyzed to assess prediction skill for SST, SAT, precipitation, sea level anomalies, sea ice concentration, and major large-scale climate variability indices. The model shows high skill in representing global SST variability and maintains consistent predictability across lead times, suggesting the role of ocean initialization in sustaining forecast skill. The geography of this skill is itself informative: it is highest, and least dependent on lead time, over the tropical Indian Ocean, where the externally forced warming dominates internal variability, and lowest over the eastern equatorial Pacific including the Niño 3.4 region, where the skill rests on the memory of the initialized ocean state and is limited by the diversity of ENSO events. Near-surface air temperature predictions also show substantial skill over both ocean and land regions, with improved performance in multi-year averaged forecasts, indicating that the system effectively captures externally forced signals and low-frequency variability relevant for near-term climate predictions. The temporal evolution of SST anomalies over global and tropical basins shows that IITM-DCPS reproduces observed long-term variability, with higher agreement at larger

spatial scales. Basin-scale SST skill is highest over the TIO (above 0.90 for the annual mean at LY1), lower over the tropical Pacific (about 0.55-0.60 at LY1), where ENSO-related internal variability dominates, and moderate over the tropical Atlantic, with better agreement in all basins at LY1-5. Analysis of major climate indices confirms that the system captures dominant modes of climate variability, including ENSO, AMO, PDO, IPO, and Indian Ocean variability, which act as important sources of decadal prediction skill. The AMO and PDO shows correlations of 0.92 or more at LY1-5, reflecting the initialized subsurface ocean heat content and their externally forced component, whereas ENSO skill at LY1 is mainly an initial-value problem, with an ACC of 0.40 for peak-season (DJF) Niño 3.4. The western pole of the IOD is predicted better than the eastern pole, so that the combined IOD index shows comparatively low skill. The leading EOF of North Pacific SST reproduces the observed PDO pattern (24.8% against 26.1% of the variance), and its PC1 correlates with the observed PC1 at 0.41 for monthly values and at 0.62 after a 12-month running mean. The evaluation of IITM-DCPS hindcasts over more than four decades shows that the system has useful capability in predicting large-scale climate variability on decadal timescales. In comparison, precipitation predictability remains more challenging, with useful skill mainly restricted to tropical regions influenced by large-scale oceanic variability. Global precipitation skill at LY1 is highest in JF and MAM (about 0.31 and 0.45) and, unlike temperature, does not improve with multi-year averaging, becoming weak or slightly negative in JJAS and OND at LY1-5. Over India, the model shows useful skill for summer monsoon (JJAS) rainfall in the first forecast year, but this skill decreases at LY1-5. Although precipitation predictability remains lower than temperature predictability due to strong internal atmospheric variability, the model appears to capture large-scale monsoon-related rainfall variability linked to tropical SST anomalies. The spatial pattern of rainfall prediction skill over India appears to be associated with large-scale ocean-atmosphere interactions, the externally forced component of the monsoon, and its synoptic-scale variability. Predictive ability remains relatively better in northwestern and peninsular India, where seasonal rainfall variability is likely influenced by the low-level jet and orographic uplift along the Western Ghats. In contrast, predictive skill is weak or negative in the CMZ and eastern India. The limited skill in the CMZ may result from both intrinsic predictability constraints and deficiencies in the representation of monsoon synoptic systems within coupled models. As low-pressure systems and depressions associated with the monsoon contribute approximately 45 to 55 percent of seasonal rainfall in central India and play a critical role in interannual rainfall variability, their formation, frequency, and trajectories exhibit significant chaotic variability, which limits deterministic predictability at multi-year lead times. This challenge is compounded by the systematic underestimation of synoptic-scale rainfall variability in coupled models; in IITM-DCPS, the synoptic (2-5 day) band accounts for 8.0-9.5% of the total JJAS rainfall variance compared to 10.9% in observations. IITM-DCPS therefore represents the synoptic-

scale rainfall variability more realistically than existing coupled models, and the limited correlation skill over the CMZ arises mainly from the chaotic interannual timing of these synoptic systems rather than from their underrepresentation. Overall, the findings indicate that the IITM-DCPS retains useful predictive skill in regions where rainfall variability is closely linked to predictable large-scale circulation. However, enhancing decadal prediction skill over central and eastern India will require improved representation of synoptic-scale monsoon systems. The representation of Indian rainfall variability therefore indicates the potential usefulness of IITM-DCPS outputs for regional climate outlooks such as the South Asian Seasonal Climate Outlook Forum (SASCOF) and EIMR rainfall predictability at multi-year timescales. Over South Asia, the SAT skill is high (ACC 0.90-0.98) and the rainfall skill is useful (ACC 0.48-0.76); over the EIMR, the SAT ACC is 0.81-0.88 at LY1 and about 0.97 at LY1-5, and rainfall skill is evident in both the annual mean and JJAS, improving at LY1-5. The model also reproduces the annual cycle of Indian rainfall, including the monsoon onset and withdrawal, with a dry bias of about 1 mm/day in July-August, and the annual cycles at LY1 and LY1-5 are nearly identical, indicating no significant drift of the simulated monsoon climatology with lead time. The persistence of skill over the tropical Indo-Pacific region highlights the importance of Pacific teleconnections, where ENSO-related variability influences Walker circulation changes, monsoon circulation strength, and rainfall distribution over the Indian subcontinent. The model reproduces the inverse ENSO-ISMR relationship during the monsoon season, but it develops earlier, during the pre-monsoon months, and is stronger than observed (about −0.70 against −0.60). In addition, the model shows good skill in representing large-scale oceanic and cryospheric variability, with sea level anomaly predictions indicating realistic simulation of basin-scale ocean heat content changes and decadal ocean circulation adjustments. Additionally, the simulation of Arctic sea ice variability highlights the role of coupled ocean-ice processes and long-term climate memory in enhancing predictability beyond seasonal timescales. Overall, these findings suggest IITM-DCPS as a capable initialized decadal prediction framework suitable for supporting regional climate outlooks, including SASCOF activities, long-range monsoon assessment, and sectoral applications related to water resources, agriculture, and coastal management. Further improving the simulation of monsoon low-pressure systems require higher resolution and an improved convection scheme, reducing the equatorward displacement of the low-level jet and the associated deficit of moisture transport into the monsoon trough, strengthening the representation of soil moisture-rainfall feedbacks, moving to an interactive treatment of aerosols, and reducing the mean-state and thermocline biases of the eastern equatorial Indian Ocean that limit IOD skill are therefore identified as the priorities for future versions of IITM-DCPS. Continued development through model physics, improved land-atmosphere interactions, and better representation of regional precipitation processes is expected to further

enhance prediction skill, particularly for Indian rainfall and associated climate impacts on decadal timescales.

Acknowledgements

The authors acknowledge the support of the Directors of IITM and NCMRWF and Secretary of Ministry of Earth Sciences (MoES), Government of India. We also acknowledge Dr. M. Rajeevan, former Secretary, MoES and Prof. Ravi Nanjundiah, former Director, IITM for their help and support in the initial period of development. We also thank CCCR, IITM for sharing the old version of IITM ESM. We thank Dr. P. Swapna, Dr. R. Krishnan and Dr. Rupa Kumar Kolli for their support. Simulations were done in Pratyush HPC. We are grateful to the National Center for Medium Range Weather Forecast (NCMRWF) for generating and providing atmospheric ICs required for the hindcast experiment.

References

Adler, R. F., and Coauthors, 2003: The Version-2 Global Precipitation Climatology Project (GPCP) Monthly Precipitation Analysis (1979–Present). *J. Hydrometeor.*, **4**, 1147–1167, https://doi.org/10.1175/1525-7541(2003)004<1147:TVGPCP>2.0.CO;2.

Annamalai, H., K. Hamilton, and K. R. Sperber, 2007: The South Asian Summer Monsoon and Its Relationship with ENSO in the IPCC AR4 Simulations. *J. Climate*, **20**, 1071–1092, https://doi.org/10.1175/JCLI4035.1.

Athanasiadis, P. J., S. Yeager, Y.-O. Kwon, L. N. Murphy, V. V. Kharin, D. M. Smith, F. Counillon, N. S. Keenlyside, H. Kim, R. Msadek, F. J. Doblas-Reyes, G. Boer, A. Bellucci, M. Kimoto, T. Mochizuki, J. Robson, N. J. Dunstone, L. Hermanson, B. Wu, Q. Wang, and E. Sanchez-Gomez, 2020: Decadal predictability of North Atlantic blocking and the NAO. npj Clim. Atmos. Sci., 3, 20, https://doi.org/10.1038/s41612-020-0120-6.

Balmaseda, M. A., H. Zuo, and Coauthors, 2019: The ECMWF Ocean Reanalysis System 5 (ORAS5). ECMWF, https://www.ecmwf.int/en/research/climate-reanalysis/ocean-reanalysis-system-5-oras5.

Barnston, A. G., M. K. Tippett, M. L. L'Heureux, S. Li, and D. G. DeWitt, 2012: Skill of real-time seasonal ENSO model predictions during 2002–11: Is our capability increasing? Bull. Amer. Meteor. Soc., 93, 631–651, https://doi.org/10.1175/BAMS-D-11-00111.1.

Bellucci, A., S. Gualdi, S. Masina, A. Storto, E. Scoccimarro, C. Cagnazzo, P. G. Fogli, E. Manzini, A. Navarra, M. Guglielmo, and M. Vichi, 2015: An assessment of a multi-model ensemble of decadal climate predictions. Climate Dyn., 44, 2787–2806, https://doi.org/10.1007/s00382-014-2164-y.

Bilbao, R., Wild, S., Ortega, P., Acosta-Navarro, J., Arsouze, T., Bretonnière, P.-A., Caron, L.-P., Castrillo, M., Cruz-García, R., Cvijanovic, I., Doblas-Reyes, F. J., Donat, M., Dutra, E., Echevarría, P., Ho, A.-C., Loosveldt-Tomas, S., Moreno-Chamarro, E., Pérez-Zanon, N., Ramos, A., Ruprich-Robert, Y., Sicardi, V., Tourigny, E., and Vegas-Regidor, J.: Assessment

of a full-field initialized decadal climate prediction system with the CMIP6 version of EC-Earth, Earth Syst. Dynam., 12, 173–196, https://doi.org/10.5194/esd-12-173-2021, 2021.

Boer, G. J., G. A. Meehl, and D. M. Smith, 2015: Toward improving decadal climate predictions. Eos, Trans. Amer. Geophys. Union, 96, 1–2, https://doi.org/10.1029/2015EO041555.

Boer, G. J., D. M. Smith, C. Cassou, G. Danabasoglu, B. P. Kirtman, Y. Kushnir, M. Kimoto, G. A. Meehl, R. Msadek, K. E. Taylor, and F. W. Zwiers, 2016: The Decadal Climate Prediction Project (DCPP) contribution to CMIP6. Geosci. Model Dev., 9, 3751–3777, https://doi.org/10.5194/gmd-9-3751-2016.

Cannon, A. J., S. R. Sobie, and T. Q. Murdock, 2015: Bias correction of GCM precipitation by quantile mapping: How well do methods preserve changes in quantiles and extremes? J. Climate, 28, 6938–6959, https://doi.org/10.1175/JCLI-D-14-00754.1.

Carmo-Costa, T., R. Bilbao, J. Robson, A. Teles-Machado, and P. Ortega, 2025: A multi-model analysis of the decadal prediction skill for the North Atlantic ocean heat content. Earth Syst. Dyn., 16, 1001–1028, https://doi.org/10.5194/esd-16-1001-2025.

Chatterjee, A., G. Anil, and L. R. Shenoy, 2022: Marine heatwaves in the Arabian Sea. Ocean Sci., 18, 639–657, https://doi.org/10.5194/os-18-639-2022.

Choi, K.-S., C.-C. Wu, and E.-J. Cha, 2010: Changes of tropical cyclone activity by Pacific–Japan teleconnection pattern in the western North Pacific. J. Geophys. Res., 115, D19114, https://doi.org/10.1029/2010JD013866.

Chowdary, J. S., D. D. Patekar, G. Srinivas, C. Gnanaseelan, and A. Parekh, 2019: Impact of the Indo-Western Pacific Ocean Capacitor mode on South Asian summer monsoon rainfall. Climate Dyn., 53, 2327–2338, https://doi.org/10.1007/s00382-019-04850-w.

Chowdary, J. S., G. Konda, A. Vibhute, A. Parekh, and C. Gnanaseelan, 2025: Potential predictability of the tropical Pacific and Indian Ocean sea surface temperature in CMIP6 DCPP models. Climate Dyn., 63, 324, https://doi.org/10.1007/s00382-025-07822-5.

Darshana, P., J. S. Chowdary, C. Gnanaseelan, A. Parekh, and G. Srinivas, 2020: Interdecadal modulation of the Indo-western Pacific Ocean Capacitor mode and its influence on Indian summer monsoon rainfall. Climate Dyn., 54, 1761–1777, https://doi.org/10.1007/s00382-019-05085-5.

Darshana, P., J. S. Chowdary, A. Parekh, and C. Gnanaseelan, 2022: Relationship between the Indo-western Pacific Ocean capacitor mode and Indian summer monsoon rainfall in CMIP6 models. Climate Dyn., 59, 393–415, https://doi.org/10.1007/s00382-021-06081-7.

Deepa, J. S., and C. Gnanaseelan, 2024: On the skill of Indo-Pacific decadal sea level predictions and its connection with skilful AMO and PDO predictions. Climate Dyn., 62, 10363–10380, https://doi.org/10.1007/s00382-024-07456-z.

Deser, C., and M. S. Timlin, 1997: Atmosphere–ocean interaction on weekly timescales in the North Atlantic and Pacific. J. Climate, 10, 393–408, https://doi.org/10.1175/1520-0442(1997)010<0393:AOIOWT>2.0.CO;2.

Doblas-Reyes, F. J., D. M. Smith, R. Bilbao, J. García-Serrano, J. M. Murphy, G. Boer, G. Danabasoglu, B. Kirtman, Y. Kushnir, M. Kimoto, G. A. Meehl, R. Msadek, K. E. Taylor, and

F. Zwiers, 2021: Decadal climate prediction: An update from the perspective of the IPCC. npj Clim. Atmos. Sci., 4, 8, https://doi.org/10.1038/s41612-021-00192-x.

Dong, C., R. Noyelle, G. Messori, and Coauthors, 2024: Indo-Pacific regional extremes aggravated by changes in tropical weather patterns. Nat. Geosci., 17, 979–986, https://doi.org/10.1038/s41561-024-01537-8.

Dwivedi, S., Mudit, and B. N. Goswami, 2026: Forecast skill of Indian summer monsoon rainfall decadal climate predictions. Theor. Appl. Climatol., 157, 595, https://doi.org/10.1007/s00704-026-06528-w.

Enayati, M., O. Bozorg-Haddad, J. Bazrafshan, S. Hejabi, and X. Chu, 2021: Bias correction capabilities of quantile mapping methods for rainfall and temperature variables. J. Water Climate Change, 12, 401–419, https://doi.org/10.2166/wcc.2020.261.

Forster, P. M., 2020: Effective radiative forcing and adjustments in CMIP6 models. Atmos. Chem. Phys., 20, 9591–9618, https://doi.org/10.5194/acp-20-9591-2020.

Frölicher, T. L., and C. Laufkötter, 2018: Emerging risks from marine heat waves. Nat. Commun., 9, 650, https://doi.org/10.1038/s41467-018-03163-6.

Goddard, L., and Coauthors, 2013: A verification framework for interannual-to-decadal prediction experiments. Climate Dyn., 40, 245–272.

Goswami, B. B., M. Deshpande, P. Mukhopadhyay, S. K. Saha, S. A. Rao, R. Murtugudde, and B. N. Goswami, 2014: Simulation of monsoon intraseasonal variability in NCEP CFSv2 and its role in the systematic bias. Climate Dyn., 43, 2725–2745, https://doi.org/10.1007/s00382-014-2089-5.

Guemas, V., S. Corti, J. García-Serrano, F. J. Doblas-Reyes, M. Balmaseda, and L. Magnusson, 2013: The Indian Ocean: The Region of Highest Skill Worldwide in Decadal Climate Prediction. *J. Climate*, **26**, 726–739, https://doi.org/10.1175/JCLI-D-12-00049.1.

Guemas, V., E. Blanchard-Wrigglesworth, M. Chevallier, J. J. Day, M. Déqué, F. J. Doblas-Reyes, N. S. Fučkar, A. Germe, E. Hawkins, S. Keeley, T. Koenigk, D. Salas y Mélia, and S. Tietsche, 2016: A review on Arctic sea-ice predictability and prediction on seasonal to decadal time-scales. Quart. J. Roy. Meteor. Soc., 142, 546–561, https://doi.org/10.1002/qj.2401.

Halder, S., A. Parekh, J. S. Chowdary, and C. Gnanaseelan, 2022: Dynamical and moist thermodynamical processes associated with Western Ghats rainfall decadal variability. npj Clim. Atmos. Sci., 5, 8, https://doi.org/10.1038/s41612-022-00232-y.

Hawkins, E., B. Dong, J. Robson, R. Sutton, and D. Smith, 2014: The Interpretation and Use of Biases in Decadal Climate Predictions. *J. Climate*, **27**, 2931–2947, https://doi.org/10.1175/JCLI-D-13-00473.1.

Henley, B.J., Gergis, J., Karoly, D.J. *et al.* A Tripole Index for the Interdecadal Pacific Oscillation. *Clim Dyn* **45**, 3077–3090 (2015). https://doi.org/10.1007/s00382-015-2525-1

Hersbach H, Bell B, Berrisford P, et al. The ERA5 global reanalysis. *Q J R Meteorol Soc*. 2020; 146: 1999–2049. https://doi.org/10.1002/qj.3803

Ho, C.K., Hawkins, E., Shaffrey, L. *et al.* Statistical decadal predictions for sea surface temperatures: a benchmark for dynamical GCM predictions. *Clim Dyn* **41**, 917–935 (2013). https://doi.org/10.1007/s00382-012-1531-9

Hobday, A. J., L. V. Alexander, S. E. Perkins, D. A. Smale, S. C. Straub, E. C. Oliver, J. A. Benthuysen, M. T. Burrows, M. G. Donat, M. Feng, and N. J. Holbrook, 2016: A hierarchical approach to defining marine heatwaves. Prog. Oceanogr., 141, 227–238, https://doi.org/10.1016/j.pocean.2015.12.014.

Huang Boyin, Peter W. Thorne, Viva F. Banzon, Tim Boyer, Gennady Chepurin, Jay H. Lawrimore, Matthew J. Menne, Thomas M. Smith, Russell S. Vose, and Huai-Min Zhang (2017): NOAA Extended Reconstructed Sea Surface Temperature (ERSST), Version 5. [indicate subset used]. NOAA National Centers for Environmental Information. doi:10.7289/V5T72FNM

Hurtt, G. C., and Coauthors, 2020: Harmonization of global land use change and management for the period 850–2100 (LUH2) for CMIP6. Geosci. Model Dev., 13, 5425–5464, https://gmd.copernicus.org/articles/13/5425/2020.

Jiang, W., P. Huang, G. Huang, and J. Ying, 2021: Origins of the excessive westward extension of ENSO SST simulated in CMIP5 and CMIP6 models. J. Climate, 34, 2839–2851, https://doi.org/10.1175/JCLI-D-20-0551.1.

Kanamitsu, M., W. Ebisuzaki, J. Woollen, S. Yang, J. J. Hnilo, M. Fiorino, and G. L. Potter, 2002: NCEP–DOE AMIP-II Reanalysis (R-2). Bull. Amer. Meteor. Soc., 83, 1631–1644, https://doi.org/10.1175/BAMS-83-11-1631.

Kirtman, B. P., and Coauthors, 2013: Near-term climate change: Projections and predictability. Climate Change 2013: The Physical Science Basis, IPCC AR5, Cambridge University Press.

Konda, G., J. S. Chowdary, C. Gnanaseelan, and Coauthors, 2023: Improvement in the skill of CMIP6 decadal hindcasts for extreme rainfall events over the Indian summer monsoon region. Sci. Rep., 13, 21737, https://doi.org/10.1038/s41598-023-48268-1.

Kushnir, Y., and Coauthors, 2019: Towards operational predictions of the near-term climate. Nat. Climate Change, 9, 94–101, https://doi.org/10.1038/s41558-018-0359-7.

Levine, A. F. Z., and M. J. McPhaden (2015), The annual cycle in ENSO growth rate as a cause of the spring predictability barrier. *Geophys. Res. Lett.*, 42, 5034–5041. doi: 10.1002/2015GL064309.

Li, T., Zhang, Y., Lu, E., & Wang, D. (2003). Relative role of dynamic and thermodynamic processes in the development of the Indian Ocean Dipole: A numerical study. *Geophysical Research Letters, 30*, 2126. https://doi.org/10.1029/2003GL018598

Lorenc, A. C., Bowler, N. E., Clayton, A. M., Pring, S. R., & Fairbairn, D. (2015). Comparison of hybrid-4DEnVar and hybrid-4DVar data assimilation methods for global NWP. Monthly Weather Review, 143(1), 212–229. https://doi.org/10.1175/mwr-d-14-00195.1

Mantua, N. J., 1999: The Pacific Decadal Oscillation. A brief overview for non-specialists. Encyclopedia of Environmental Change.

Marcheggiani, A., J. Robson, P. Monerie, and Coauthors, 2023: Decadal predictability of the North Atlantic eddy-driven jet in winter. Geophys. Res. Lett., 50, e2022GL102071, https://doi.org/10.1029/2022GL102071.

Meehl, G. A., L. Goddard, G. Boer, and Coauthors, 2014: Decadal climate prediction: An update from the trenches. Bull. Amer. Meteor. Soc., 95, 243–267, https://doi.org/10.1175/BAMS-D-12-00241.

Merryfield, W. J., and Coauthors, 2020: Current and emerging developments in subseasonal to decadal prediction. Bull. Amer. Meteor. Soc., 101, E869–E896, https://doi.org/10.1175/BAMS-D-19-0037.1.

Nitta, T., 1987: Convective activities in the tropical western Pacific and their impacts on the Northern Hemisphere summer circulation. J. Meteor. Soc. Japan, 65, 373–390, https://doi.org/10.2151/jmsj1965.65.3_373.

Noh, K. M., H. G. Lim, and J. S. Kug, 2022: Global chlorophyll responses to marine heatwaves in satellite ocean color. Environ. Res. Lett., 17, 064034, https://doi.org/10.1088/1748-9326/ac70ec.

Paul, B., Feba, F., Ashok, K., Francis, P. A., & Pentakota, S. (2026). The prediction skill of Indian Ocean dipole mode in DCPP-CMIP6 decadal hindcast models. *Environmental Research Communications, 8*(4), 045019. https://doi.org/10.1088/2515-7620/ae59f5

Peings, Y., and H. Douville, 2010: Influence of the Eurasian snow cover on the Indian summer monsoon variability in observed climatologies and CMIP3 simulations. Climate Dyn., 34, 269–291.

Power, S., T. Casey, C. Folland, and Coauthors, 1999: Inter-decadal modulation of the impact of ENSO on Australia. Climate Dyn., 15, 319–324, https://doi.org/10.1007/s003820050284.

Prasad, V. S., C. J. Johny, and J. S. Sodhi. 2016. “Impact of 3D Var GSI-ENKF Hybrid Data Assimilation System.” Journal of Earth System Science 125 (8): 1509–1521. https://doi.org/10.1007/s12040-016-0761-3.

Qian, W., and H. H. Chang, 2021: Projecting health impacts of future temperature: A comparison of quantile-mapping bias-correction methods. Int. J. Environ. Res. Public Health, 18, 1992, https://doi.org/10.3390/ijerph18041992.

Rajesh, P. V., R. Panda, C. Gnanaseelan, R. Pai, R. Kakatkar, D. Patekar, J. S. Deepa, A. G. Prajeesh, A. K. Sharma, T. S. Fousiya, S. Halder, S. Sebastian, A. Parekh, and S. Pramanik, 2026: Assessment of the IITM decadal climate prediction system for interannual to decadal climate variability and Indian Summer Monsoon teleconnections. Research Rep. RR-148, Indian Institute of Tropical Meteorology, Pune, ISSN 0252-1075, https://www.tropmet.res.in/~lip/Publication/Rr-pdf/RR-148.pdf.

Rasmusson, E. M., and T. H. Carpenter, 1982: Variations in tropical sea surface temperature and surface wind fields associated with the Southern Oscillation/El Niño. Mon. Wea. Rev., 110, 354–384, https://doi.org/10.1175/1520-0493(1982)110<0354:VITSST>2.0.CO;2.

Reifenberg, S. F., and H. F. Goessling, 2022: Predictability of Arctic sea ice drift in coupled climate models. Cryosphere, 16, 2927–2946, https://doi.org/10.5194/tc-16-2927-2022.

Reynolds, R. W., T. M. Smith, C. Liu, D. B. Chelton, K. S. Casey, and M. G. Schlax, 2007: Daily high-resolution-blended analyses for sea surface temperature. J. Climate, 20, 5473–5496, https://doi.org/10.1175/2007JCLI1824.1.

Richter, I., 2015: Climate model biases in the eastern tropical oceans: Causes, impacts and ways forward. Wiley Interdiscip. Rev.: Climate Change, 6, 345–358, https://doi.org/10.1002/wcc.338.

Saji, N. H., Goswami, B. N., Vinayachandran, P. N., & Yamagata, T. (1999). A dipole mode in the tropical Indian Ocean. *Nature, 401*, 360–363. https://doi.org/10.1038/43854

Salinger, M.J., Renwick, J.A. and Mullan, A.B. (2001), Interdecadal Pacific Oscillation and South Pacific climate. Int. J. Climatol., 21: 1705-1721. https://doi.org/10.1002/joc.691

Simpson, I. R., S. G. Yeager, K. A. McKinnon, and C. Deser, 2019: Decadal predictability of late winter precipitation in western Europe through an ocean–jet stream connection. Nat. Geosci., 12, 613–619, https://doi.org/10.1038/s41561-019-0391-x.

Smith, C. J., R. J. Kramer, G. Myhre, and Coauthors, 2015: Towards predictive understanding of regional climate change. Nat. Climate Change, 5, 921–930, https://doi.org/10.1038/nclimate2689.

Smith, D. M., R. Eade, A. A. Scaife, and Coauthors, 2019: Robust skill of decadal climate predictions. npj Clim. Atmos. Sci., 2, 13, https://doi.org/10.1038/s41612-019-0071-y.

Srinivas, G., J. S. Chowdary, Y. Kosaka, C. Gnanaseelan, A. Parekh, and K. V. S. R. Prasad, 2018: Influence of the Pacific–Japan pattern on Indian summer monsoon rainfall. J. Climate, 31, 3943–3958, https://doi.org/10.1175/JCLI-D-17-0408.1.

Sun, X., R. G. Greatbatch, W. Park, and M. Latif, 2010: Two major modes of variability of the East Asian summer monsoon. Quart. J. Roy. Meteor. Soc., 136, 829–841, https://doi.org/10.1002/qj.635.

Teng, H., G. A. Meehl, G. Branstator, and Coauthors, 2017: Initialization shock in CCSM4 decadal prediction experiments. Past Global Changes Mag., 25, 41–46, https://doi.org/10.22498/pages.25.1.41.

Tokinaga, H., S. Xie, A. Timmermann, S. McGregor, T. Ogata, H. Kubota, and Y. M. Okumura, 2012: Regional patterns of tropical Indo-Pacific climate change: Evidence of the Walker circulation weakening. J. Climate, 25, 1689–1710, https://doi.org/10.1175/JCLI-D-11-00263.1.

Tong, Y., X. Gao, Z. Han, Y. Xu, Y. Xu, and F. Giorgi, 2021: Bias correction of temperature and precipitation over China for RCM simulations using the QM and QDM methods. Climate Dyn., 57, 1425–1443, https://doi.org/10.1007/s00382-020-05447-4.

Torrence, C. and Webster, P.J. (1998), The annual cycle of persistence in the El Nño/Southern Oscillation. Q.J.R. Meteorol. Soc., 124: 1985-2004. https://doi.org/10.1002/qj.49712455010

Toth, Z., and E. Kalnay, 1993: Ensemble forecasting at NMC: The generation of perturbations. Bull. Amer. Meteor. Soc., 74, 2317–2330.

Vibhute, A., S. Halder, P. Singh, and Coauthors, 2020: Decadal variability of tropical Indian Ocean sea surface temperature and its impact on the Indian summer monsoon. Theor. Appl. Climatol., 141, 551–566, https://doi.org/10.1007/s00704-020-03216-1.

Wallace, J. M., C. Smith, and C. S. Bretherton, 1992: Singular value decomposition of wintertime sea surface temperature and 500-mb height anomalies. J. Climate, 5, 561–576, https://doi.org/10.1175/1520-0442(1992)005<0561:SVDOWS>2.0.CO;2.

Wang, X., & Lei, T. (2014). GSI-based four-dimensional ensemble–variational (4DEnsVar) data assimilation: Formulation and single-resolution experiments with real data for NCEP Global Forecast System. Monthly Weather Review, 142(9), 3303–3325. https://doi.org/10.1175/mwr-d-13-00303.1

Wang, L.-C., and Y.-S. Lin, 2023: A potential reason for a more CP El Niño-like SSTA performance in CMIP6 simulations. *Geophys. Res. Lett.*, **50**, e2023GL105092, https://doi.org/10.1029/2023GL105092

Webster, P. J., and S. Yang, 1992: Monsoon and ENSO: Selectively interactive systems. Quart. J. Roy. Meteor. Soc., 118, 877–926.

World Meteorological Organization (WMO), 2021: *Guidelines for the Submission of WMO Climatological Standard Normals: Collection for 1991–2020*. World Meteorological Organization, Geneva, Switzerland.

Xie, P., and P. A. Arkin, 1997: Global precipitation: A 17-year monthly analysis based on gauge observations, satellite estimates, and numerical model outputs. Bull. Amer. Meteor. Soc., 78, 2539–2558.

Xie, S.-P., Y. Kosaka, Y. Du, K. Hu, J. S. Chowdary, and G. Huang, 2016: Indo-western Pacific Ocean capacitor and coherent climate anomalies in post-ENSO summer: A review. Adv. Atmos. Sci., 33, 411–432, https://doi.org/10.1007/s00376-015-5192-6.

Yeager, S. G., A. R. Karspeck, and G. Danabasoglu, 2015: Predicted slowdown in the rate of Atlantic sea ice loss. Geophys. Res. Lett., 42, 10,704–10,713, https://doi.org/10.1002/2015GL065364.

Yoon, J.-H., and T.-C. Chen, 2005: Water vapor budget of the Indian monsoon depression. Tellus A, 57, 770–782.

Zhang, Y., J. M. Wallace, and D. S. Battisti, 1997: ENSO-like interdecadal variability: 1900–93. J. Climate, 10, 1004–1014, https://doi.org/10.1175/1520-0442(1997)010<1004:ELIV>2.0.CO;2.

Figures

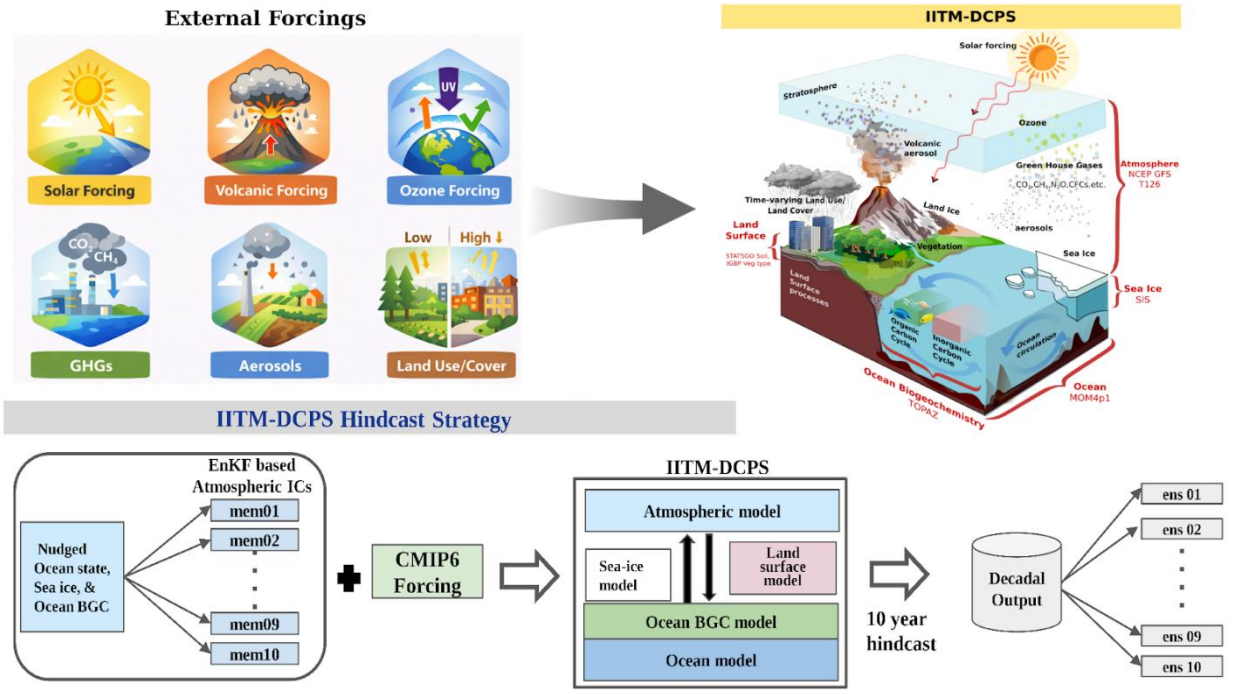


Figure 1. Schematic illustrates the key physical components of the IITM-DCPS, coupled processes, external forcings and strategy used for hindcast generation.

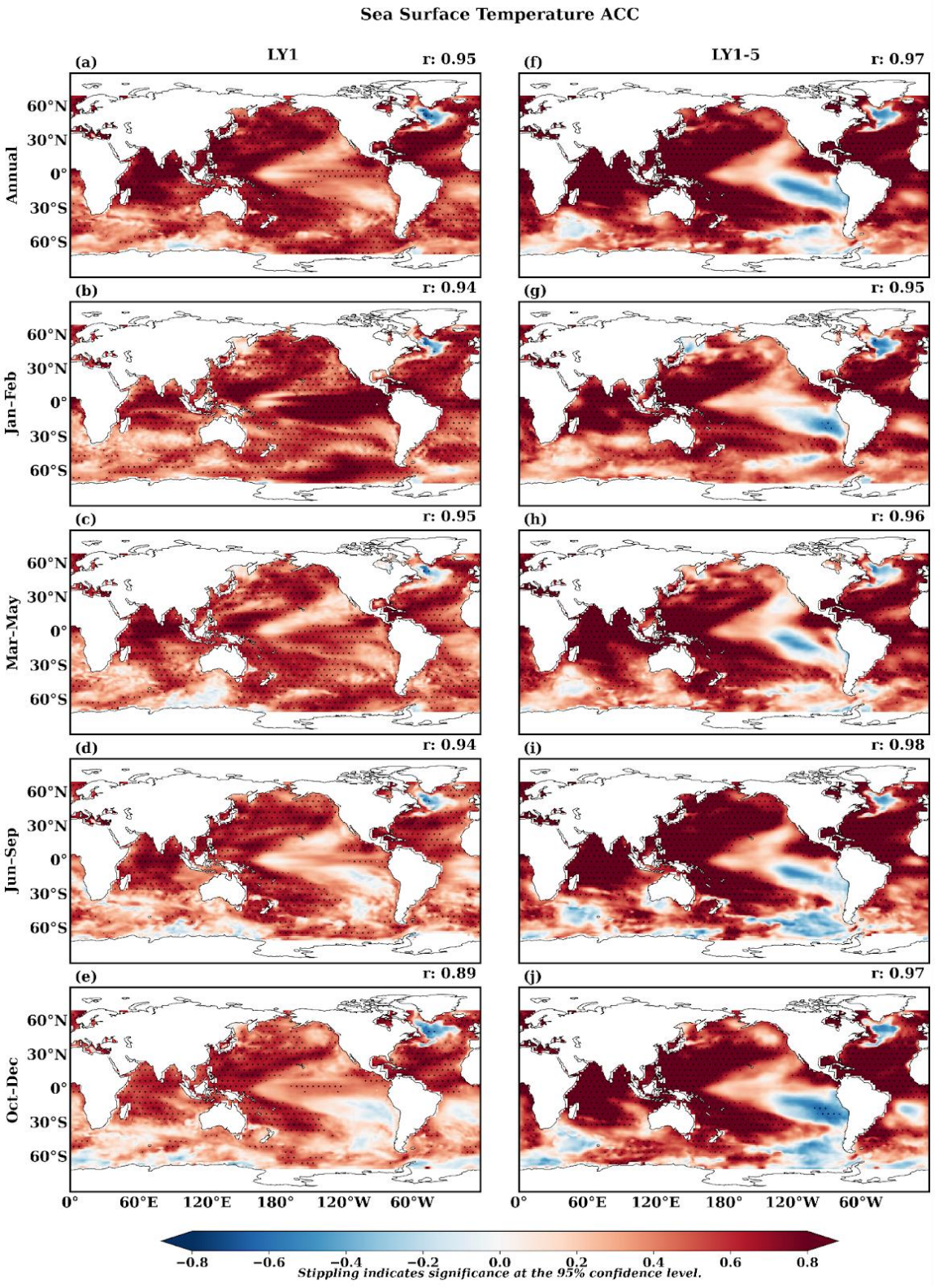


Figure 2. Spatial distribution of the ACC for SST between the IITM-DCPS hindcasts and observations for the global annual mean and seasonal averages (JF, MAM, JJAS, and OND) for LY1 (a-e) and LY1-5(f-j), stippling indicates significance at the 95% confidence level.

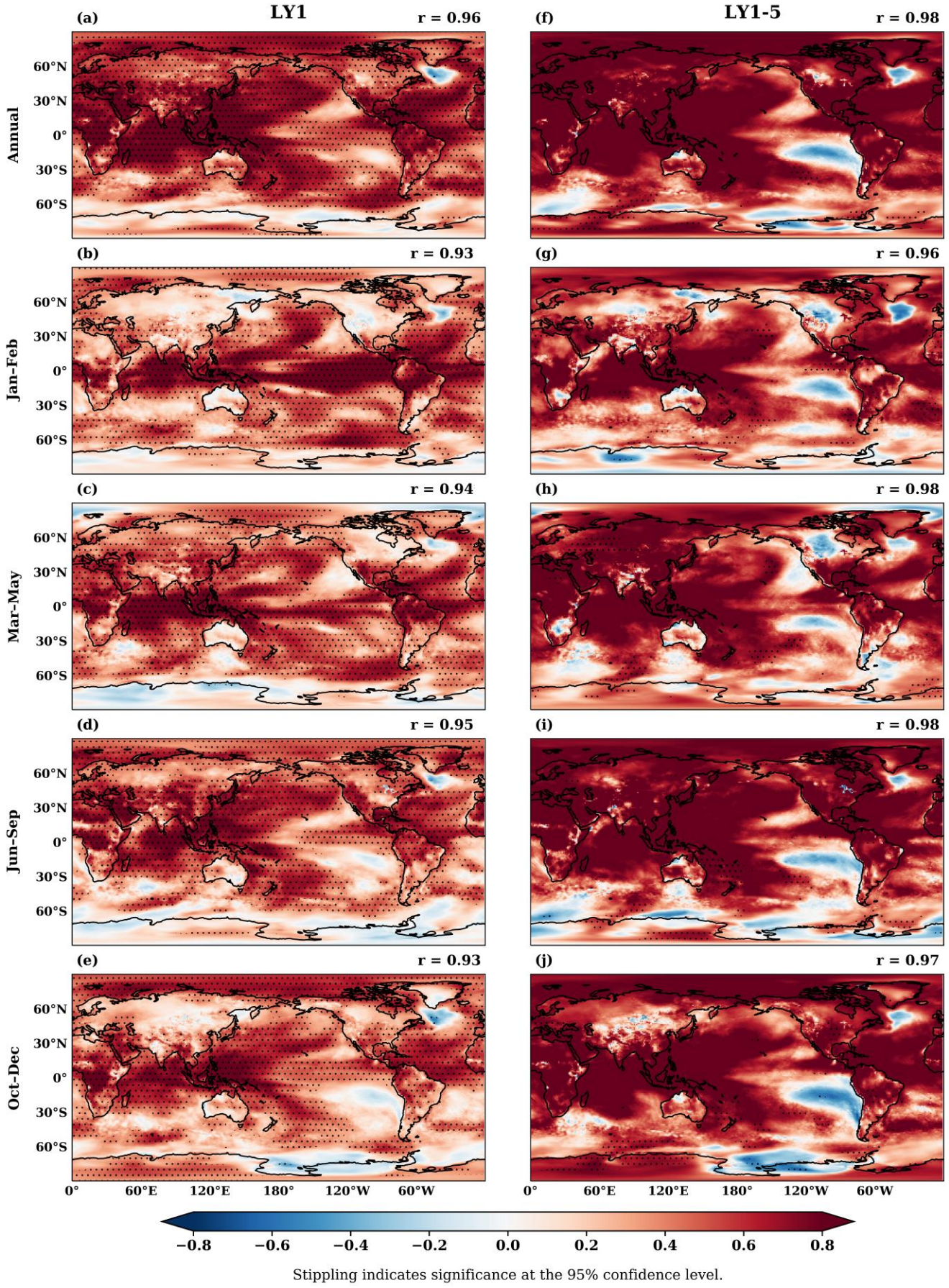


Figure 3. Same as figure 2 but for Near-Surface Air Temperature.

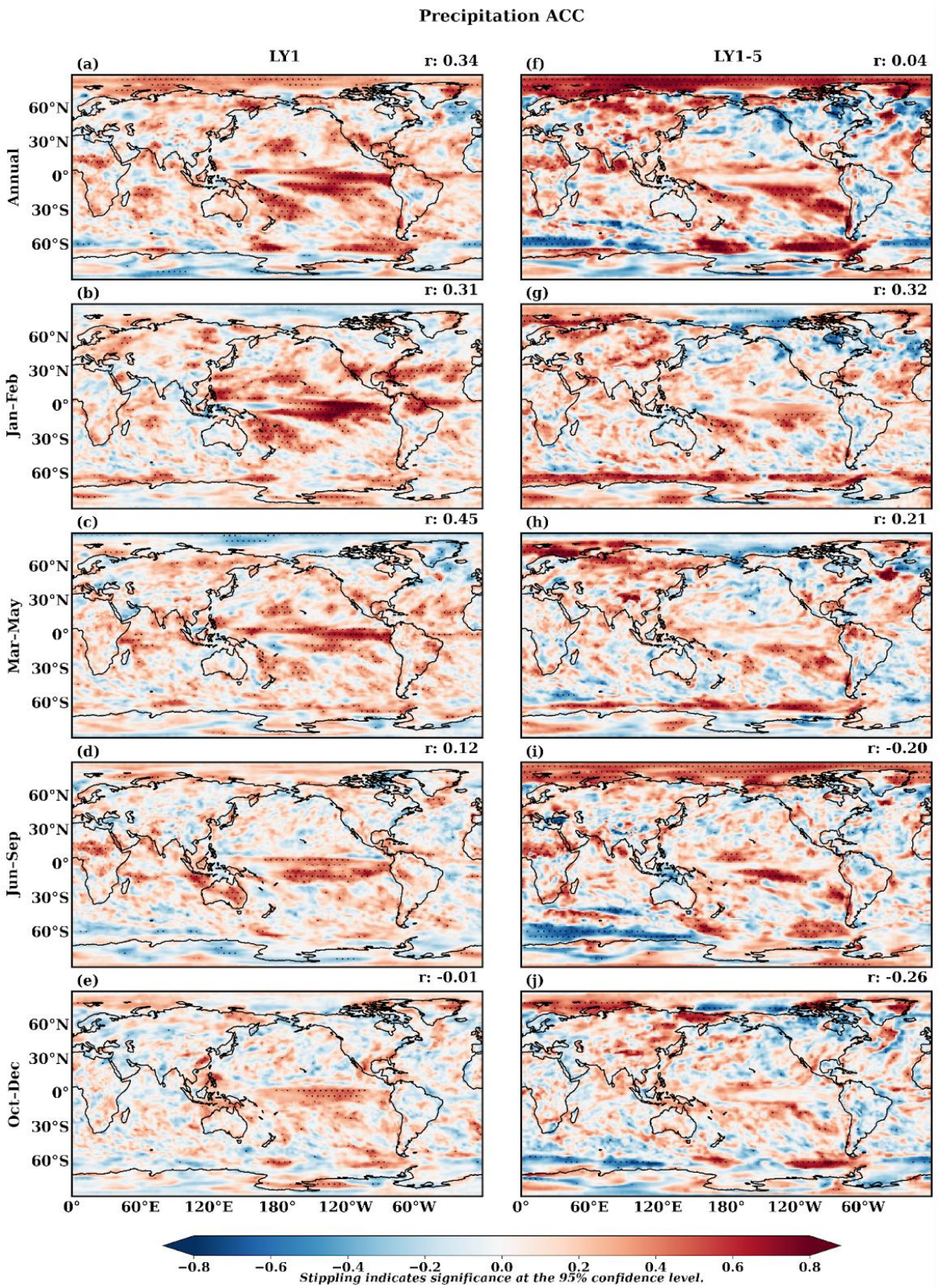


Figure 4. Same as figure 2 but for Precipitation.

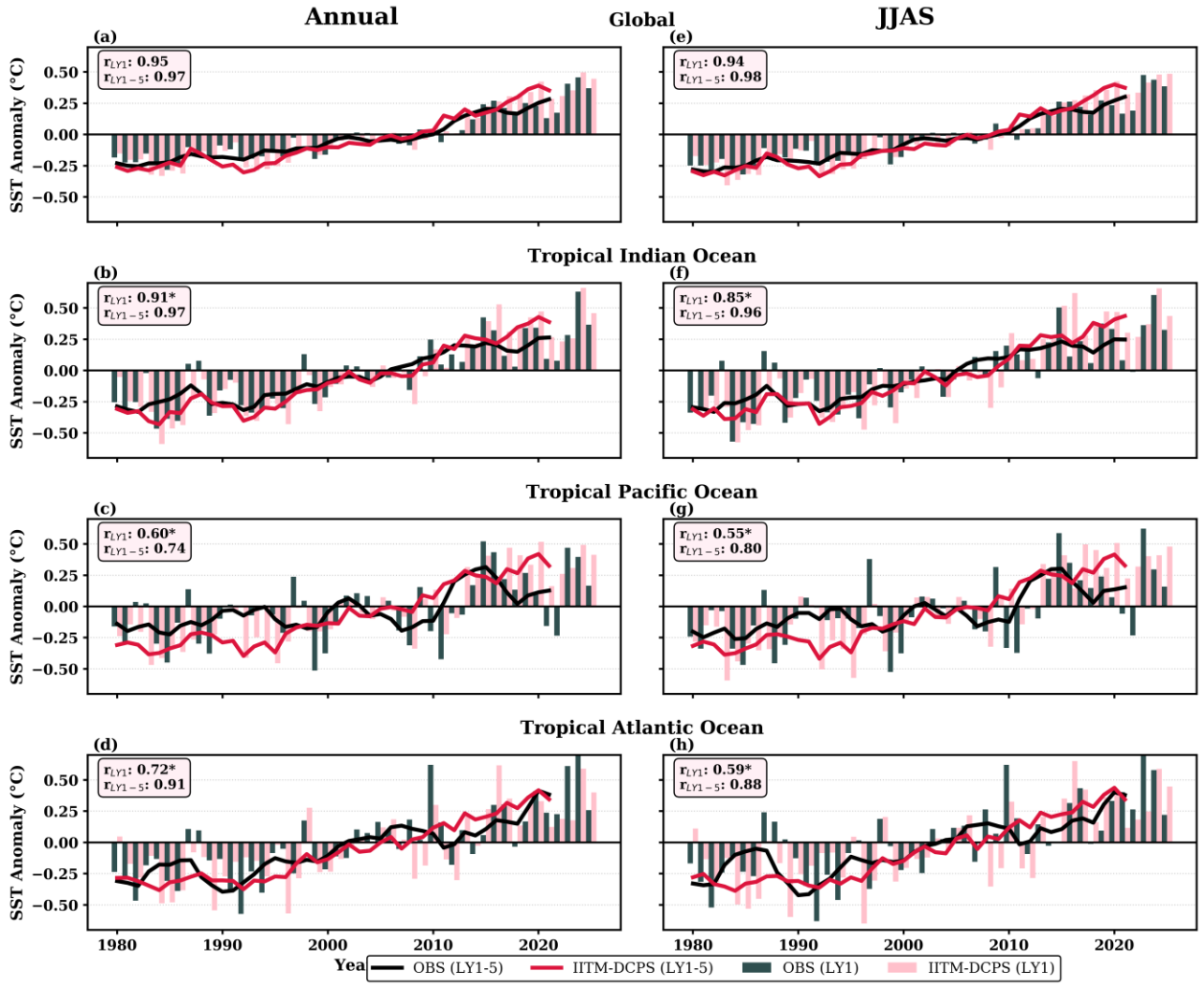


Figure 5. Time-series of SST anomalies from the IITM-DCPS and ERSSTv5 observations for Global Ocean, TIO, TPO and TAO for the Annual mean (a-d) and JJAS season (e-h). Pink bars represent LY1 hindcasts, grey bars represent observations, red lines indicate LY1-5 hindcasts, and black lines represent observations. rly1 and rly1-5 denotes the correlation values, '*' indicates correlations that are statistically significant at 95% confidence level.

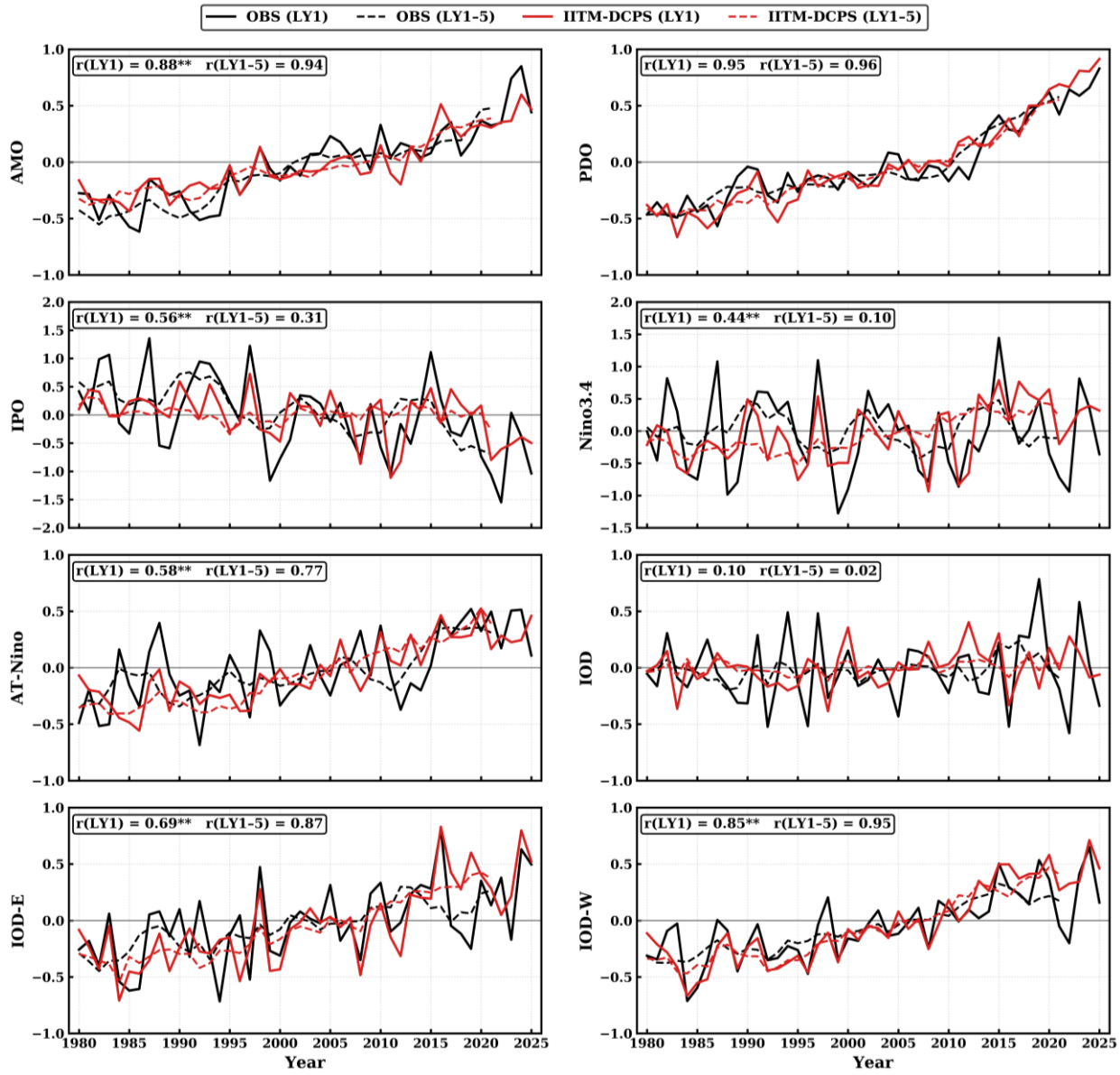


Figure 6. Temporal evolution of SST base climate indices for annual between hindcast (red) and Observation (black) for LY1(solid) and LY1-5 (dashed line) and the correlation coefficient (r) given in each plot, '*' indicates a correlation significance at 95% confidence level.

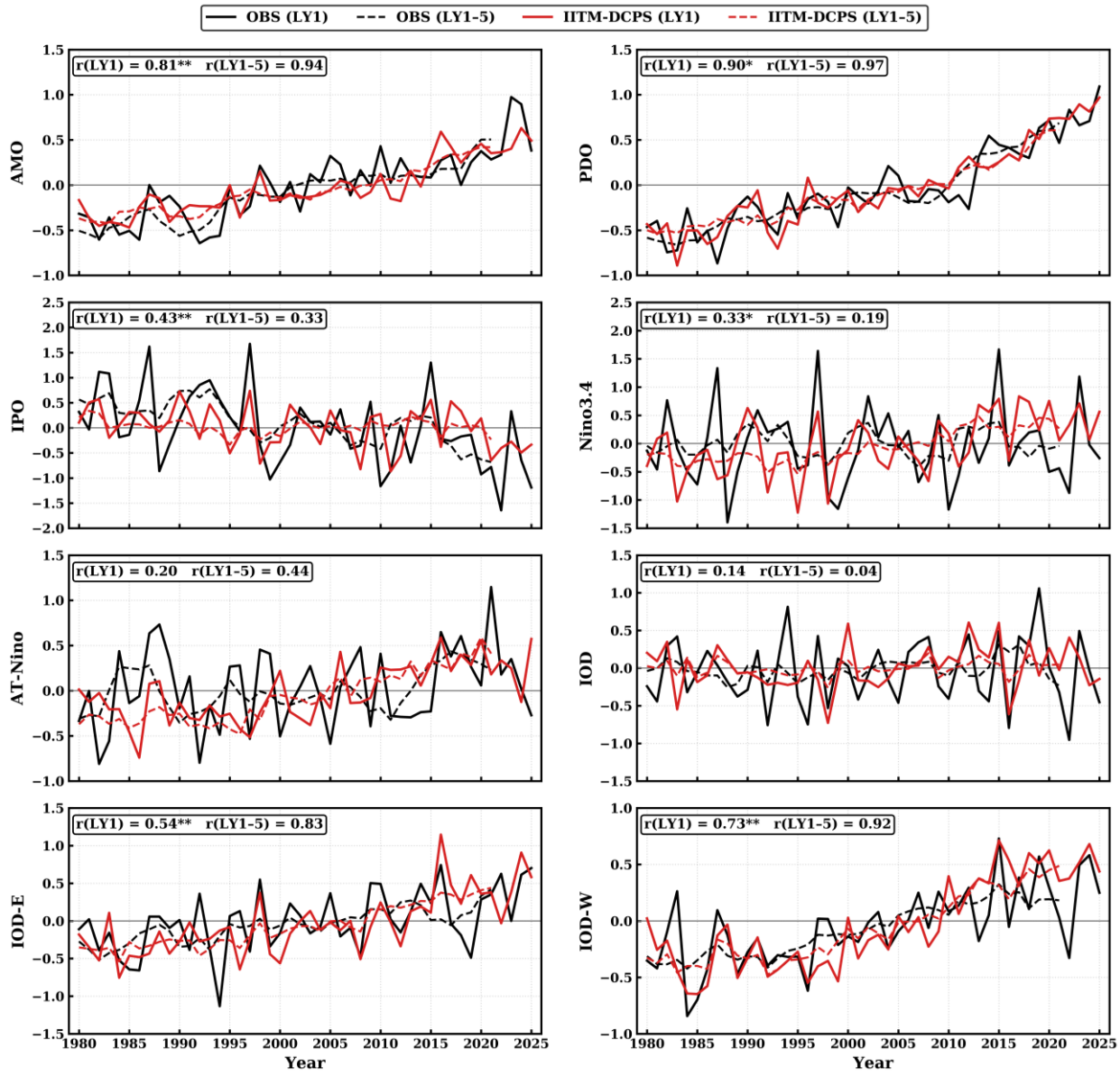


Figure 7. Same as figure 6 but for summer-monsoon season (JJAS).

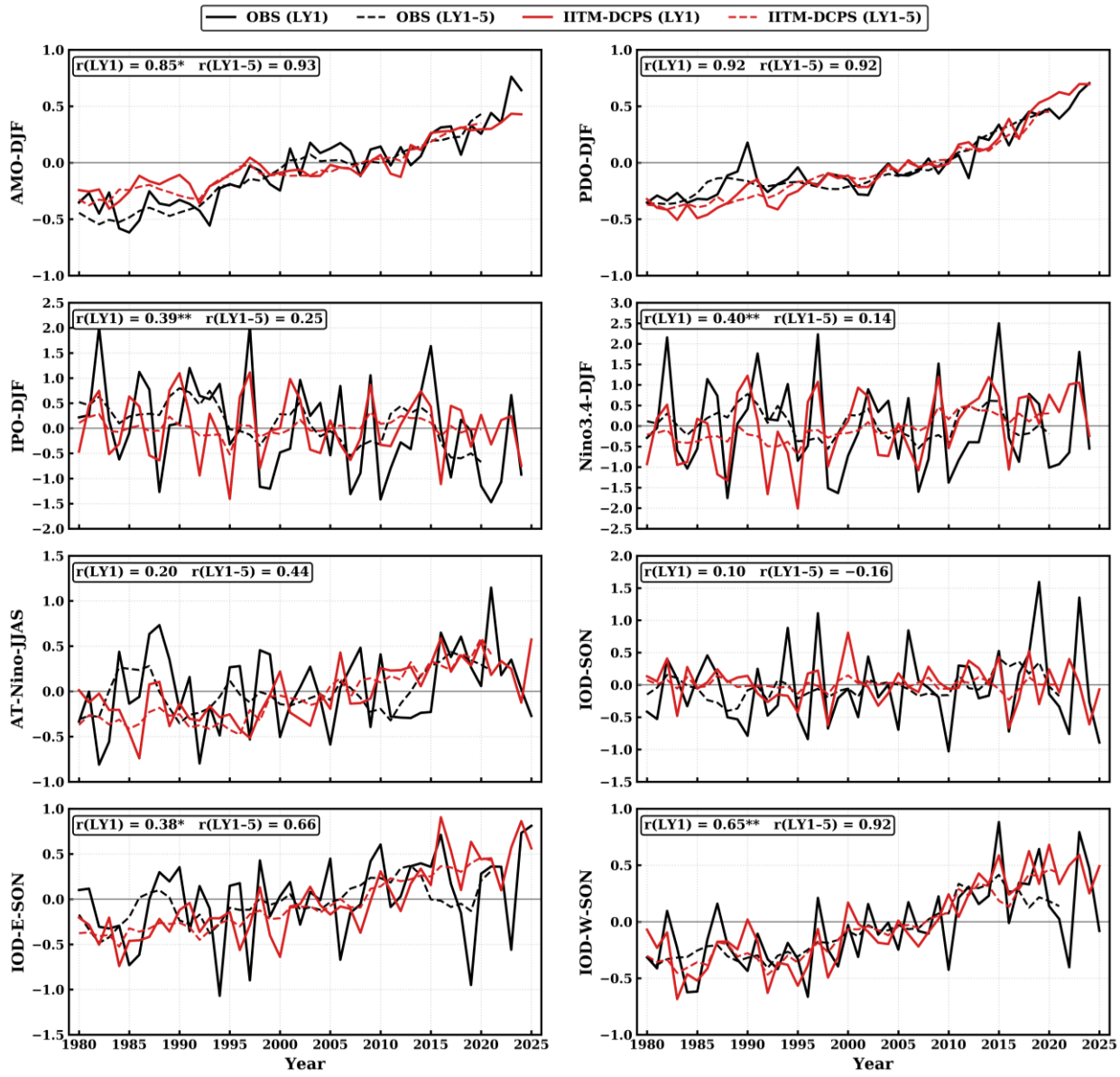


Figure 8. Same as figure 6 but for respective peak season.

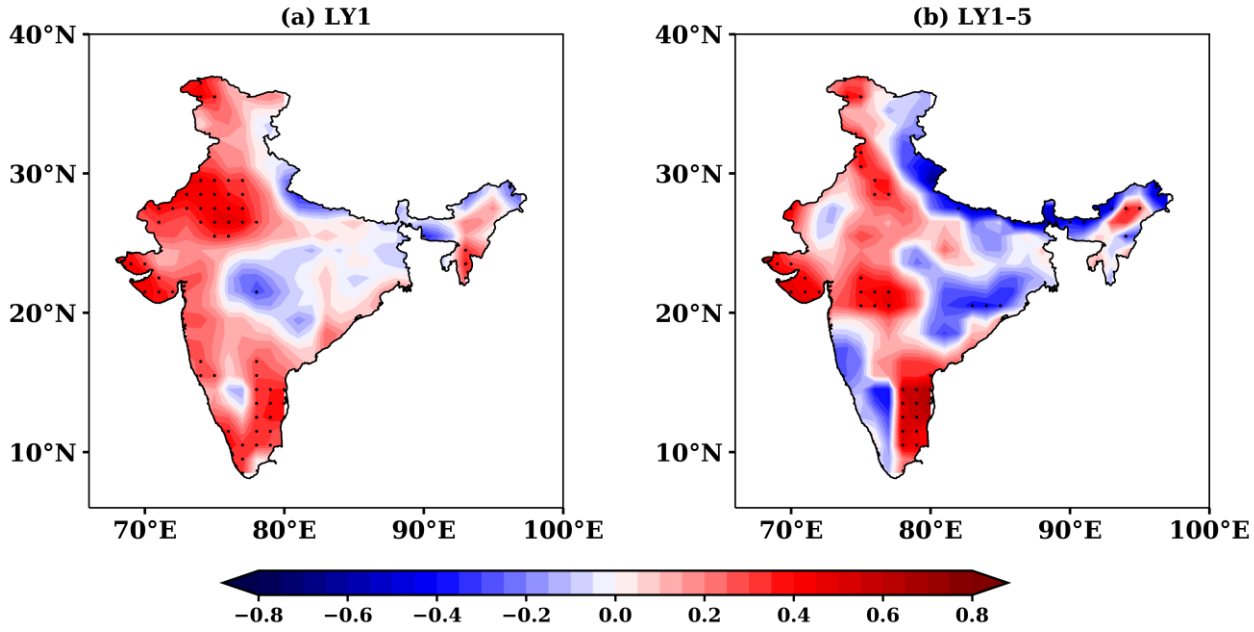


Figure 9. Spatial distribution of ACC of summer (JJAS) rainfall over India for (a) LY1 and (b) LY1-5. Stippling denotes regions significance at 95% confidence level.

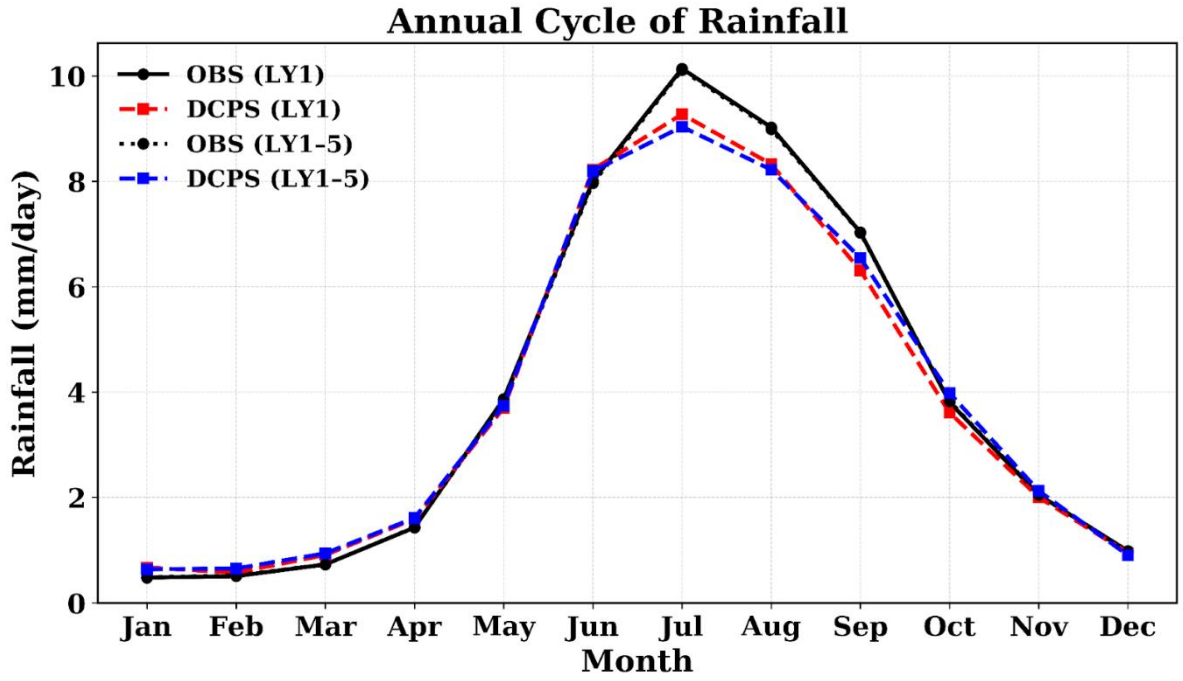


Figure 10. Annual cycle rainfall over Indian domain (72°E-98°E, 10°N-32°N) for LY1 (DCPS:red, OBS:black_solid line) and LY1-5 (DCPS: blue, OBS: black_dashed line).

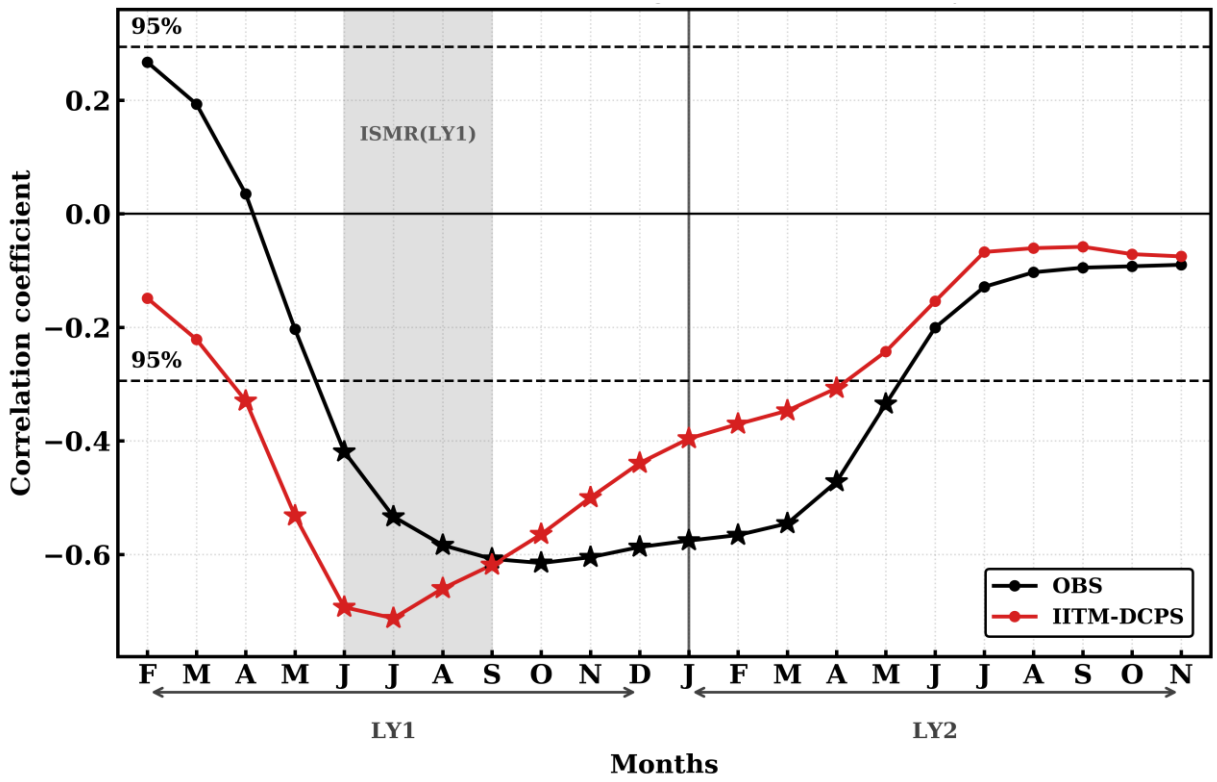


Figure 11. Lead-lag correlation between ISMR and monthly Nino3.4 SST anomalies. Red and Black lines represent Model and Observations, respectively. Horizontal dashed lines indicating the 95% significance confidence level. Markers (⋆) identify months where the correlation is statistically significant ($p<0.05$).

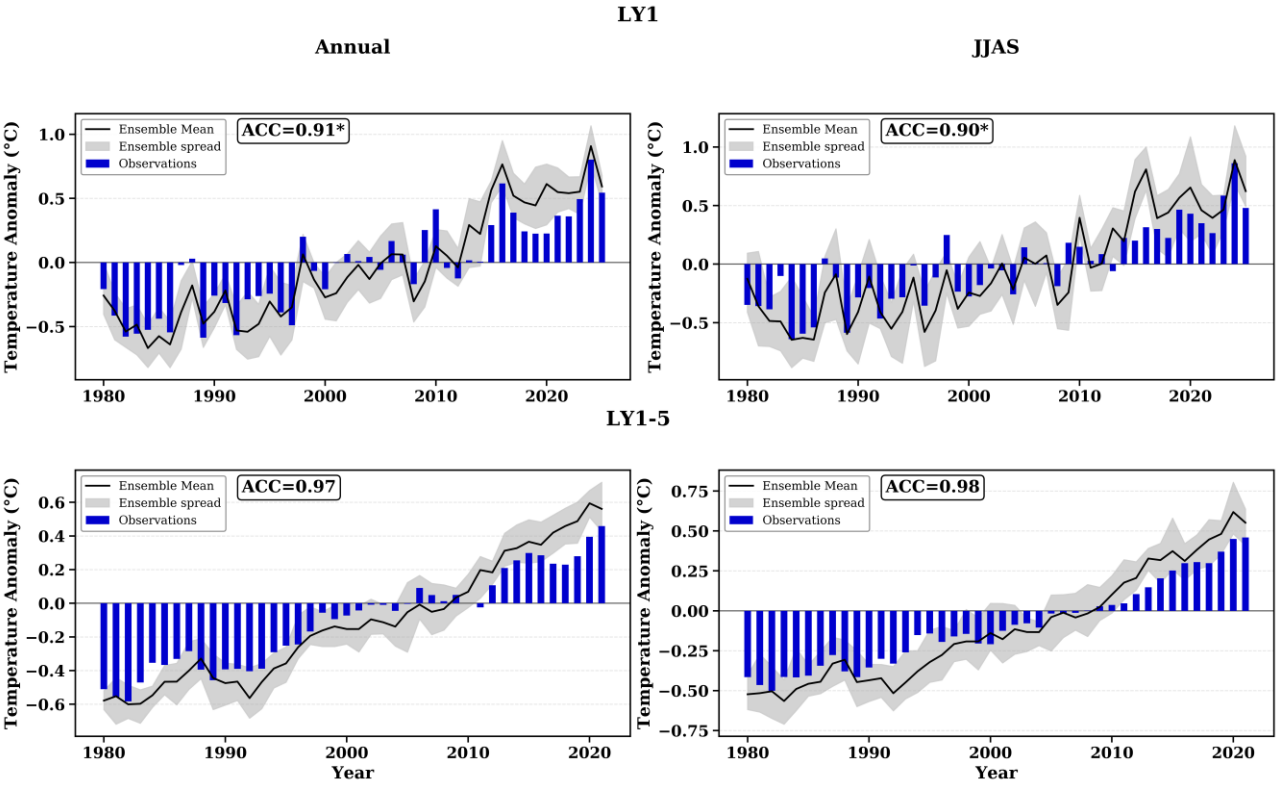


Figure 12. Time series of SAT anomalies over the South Asian region, ensemble mean predictions (black line), observations (blue bars), and ensemble spread (grey shading). Panels show Annual and

summer (JJAS) rainfall anomalies for LY1 (top panels) and LY1-5 (bottom panels). The ACC between predictions and observations is shown in each plot, '*' indicates a correlation significance at 95% confidence level.

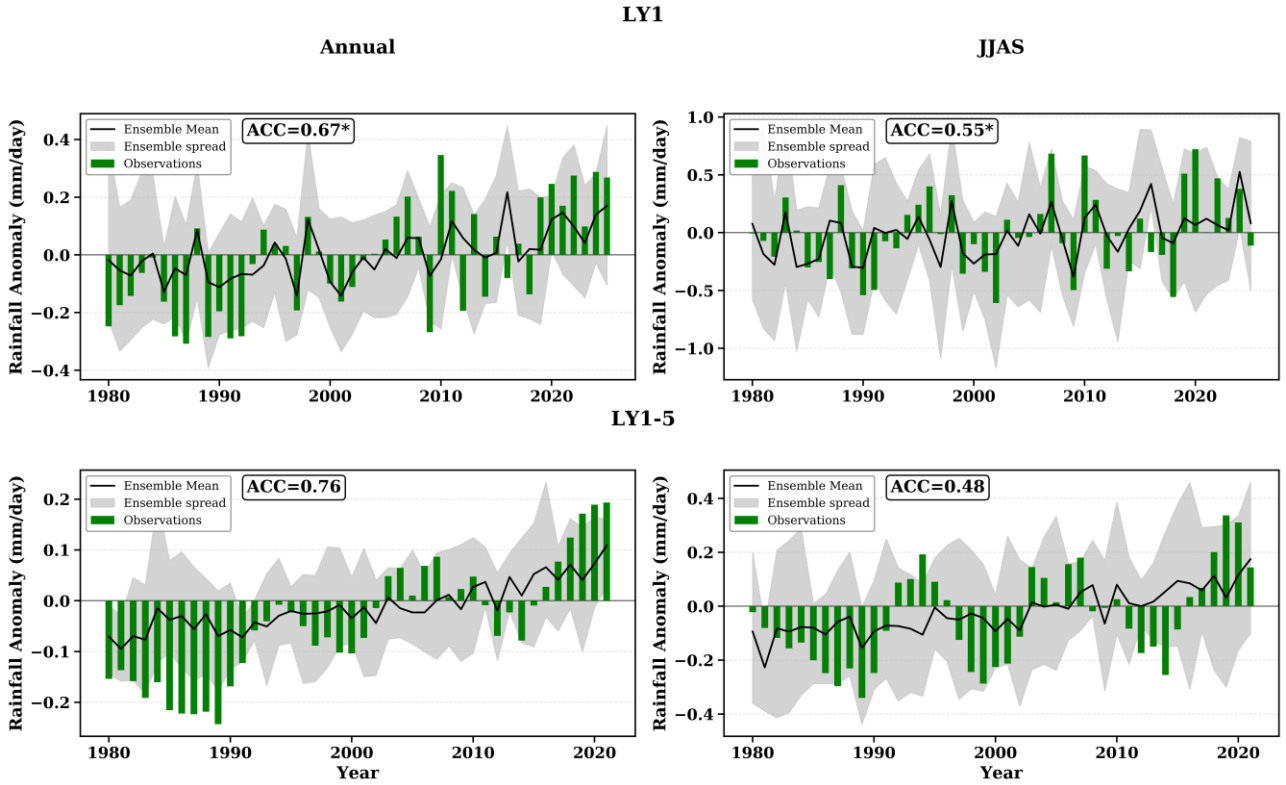


Figure 13. Same as Figure 12 but for Rainfall (Precipitation)

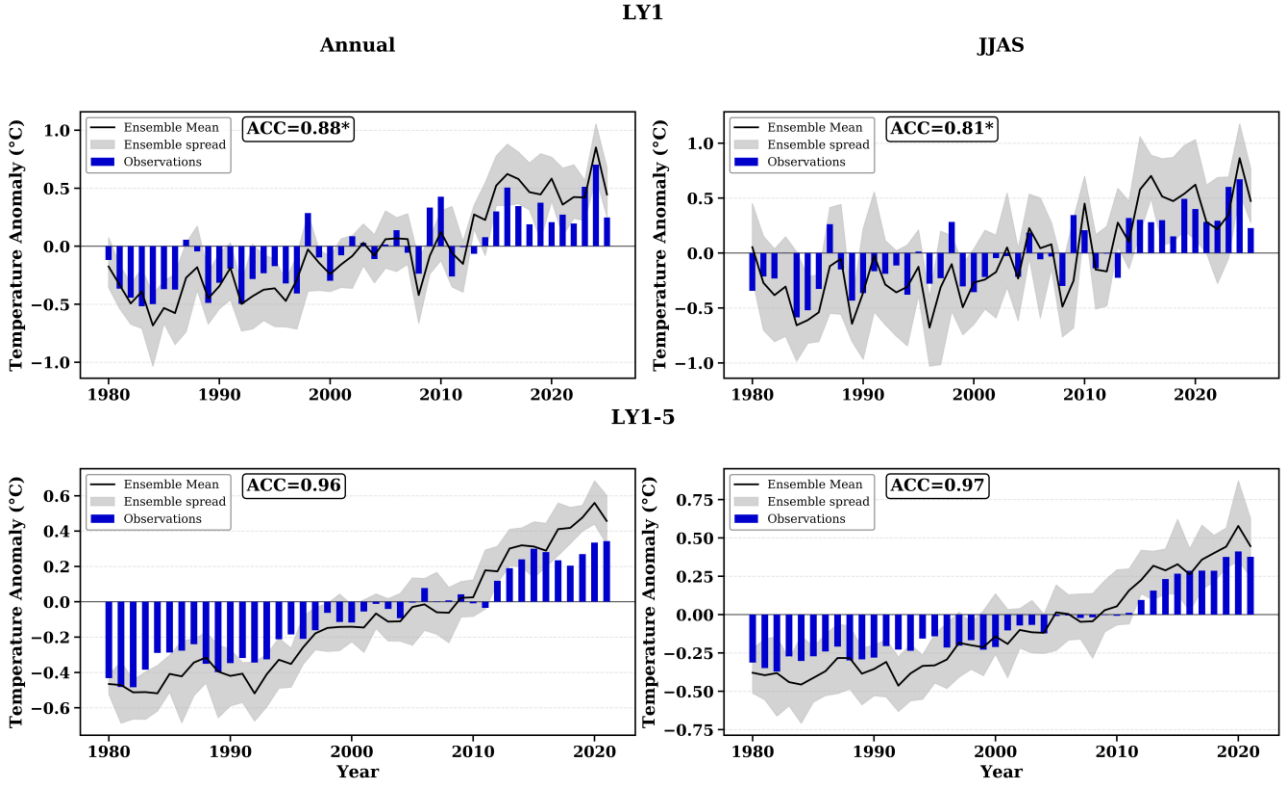


Figure 14. Same as the Figure 12 but for Extended Indian Monsoon Region (EIMR).

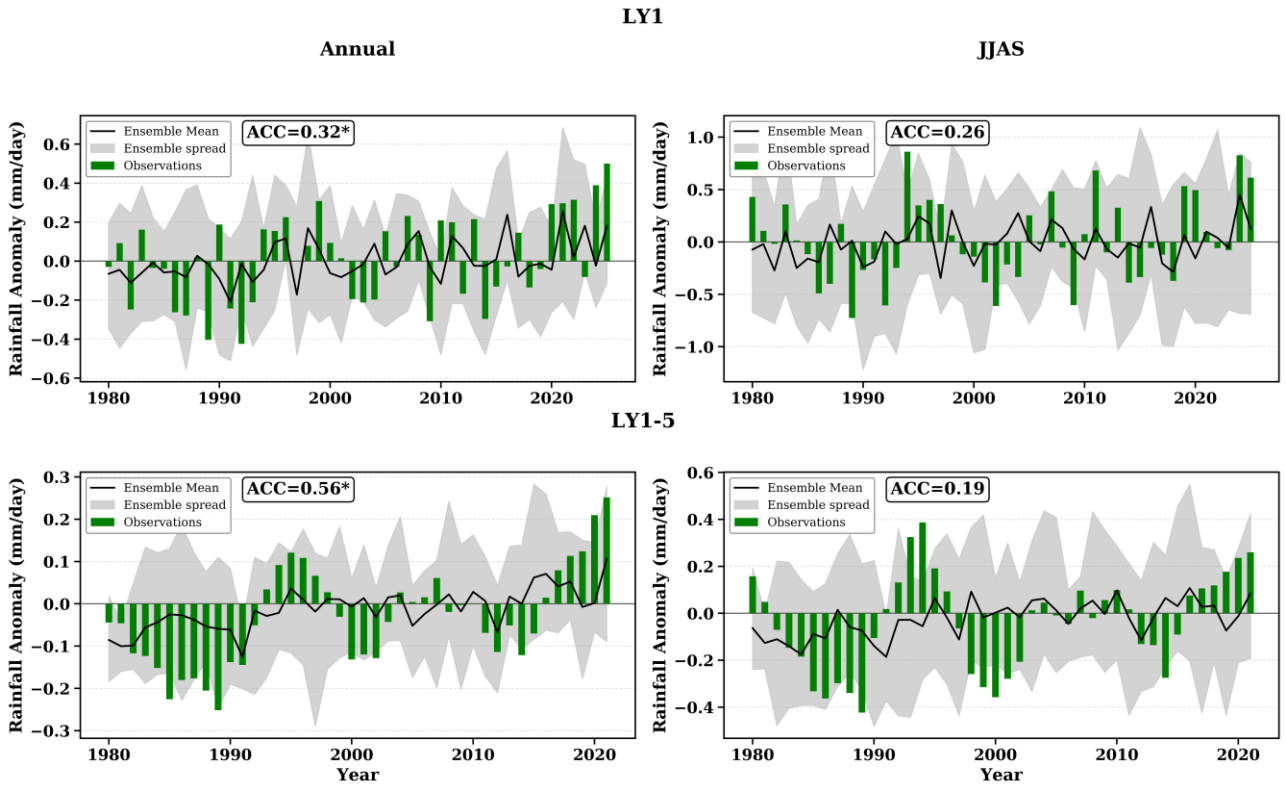


Figure 15. Same as Figure 13 but for EIMR Precipitation.

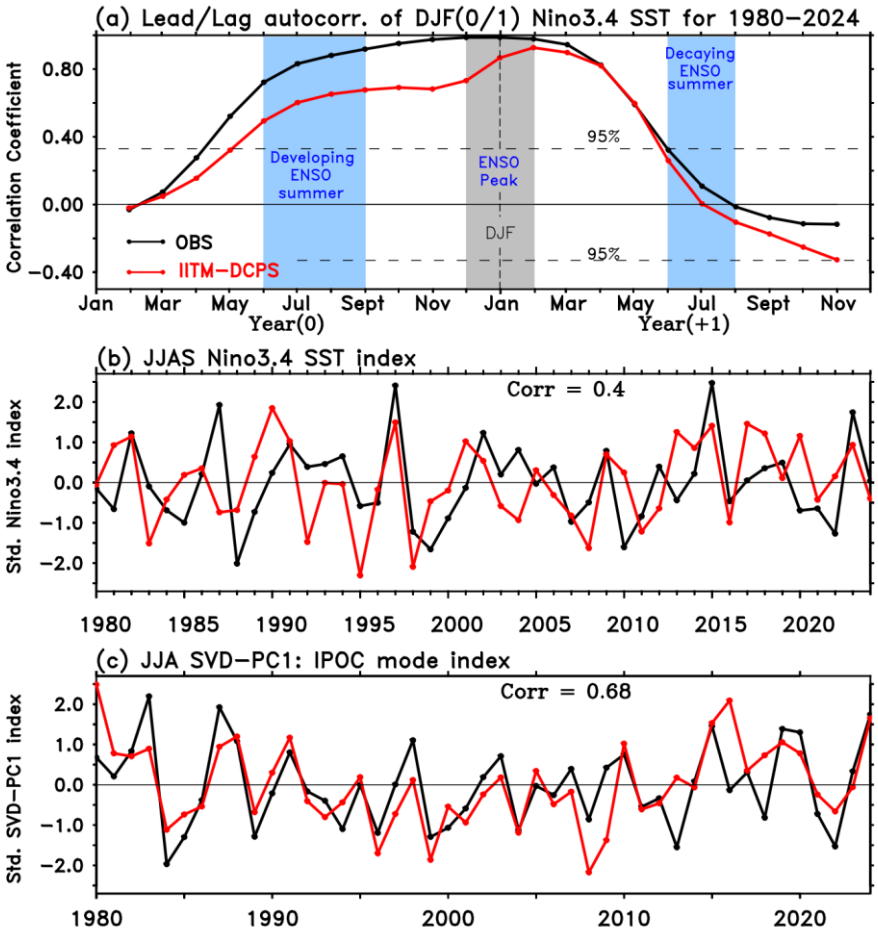


Figure 16: For OBS and IITM-DCPS lead year 1: (a) Lead-lag correlation coefficients between D(0)JF(1) Niño 3.4 with monthly Niño 3.4 SST. Dashed horizontal (vertical) lines indicate 95% significant correlation value (leading years' partition), (b) JJAS Niño 3.4 SST index (Developing ENSO summer), and (c) JJA SVDPC1/IPOC index (Decaying ENSO summer).

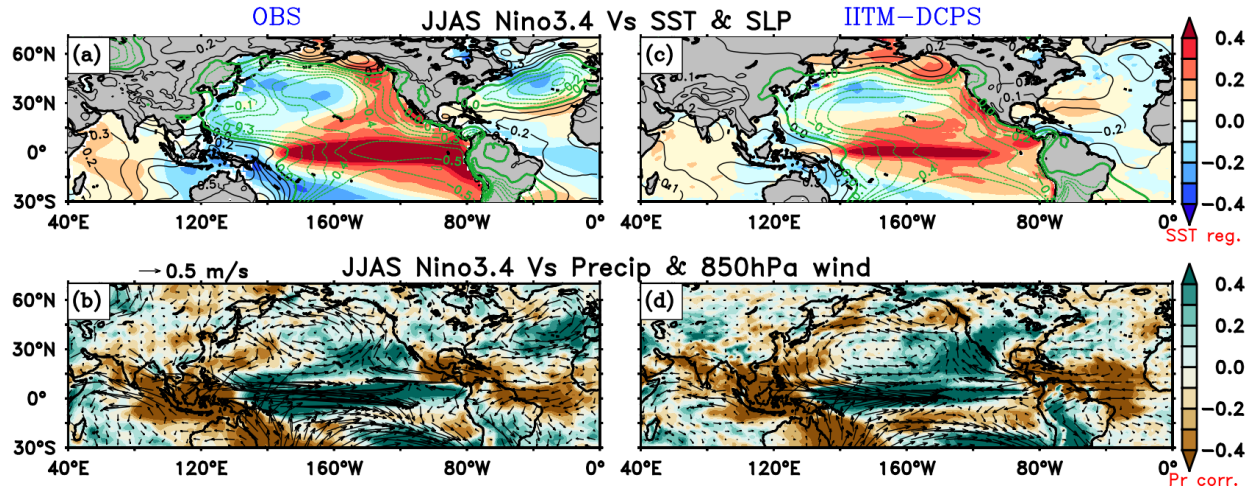


Figure 17. (a,c) JJAS Niño 3.4 regression upon JJAS SST(shaded; degC) and SLP(contours; hPa) anomaly (b,d) JJAS Niño 3.4 correlation with precipitation (shaded; mm/day) and regression upon 850 hPa wind (vectors; m/s) anomalies in OBS and IITM-DCPS model for LY1. Solid (dashed) black (green) contours represent positive (negative) SLP anomalies and thick solid green contour is zero SLP value in (a) and (c).

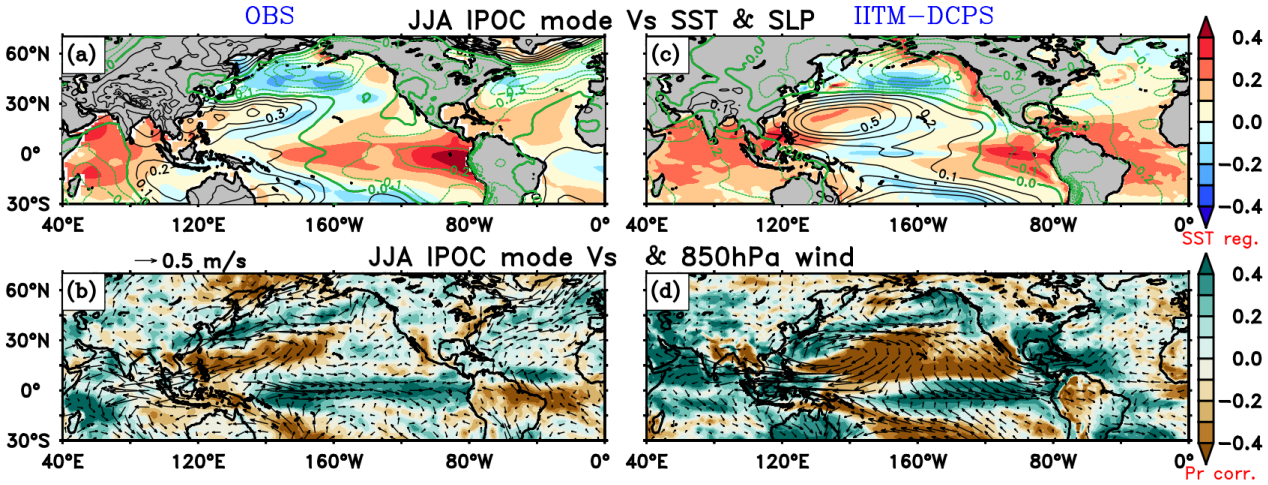


Figure 18. (a,c) JJA SVD-PC1 regression upon JJA SST(shaded; degC) and SLP(contours; hPa) (b,d) JJA SVD-PC1 correlation with precipitation (shaded; mm/day) and regression upon 850 hPa wind (vectors; m/s) anomalies in OBS and IITM-DCPS model for LY1. Solid (dashed) black (green) contours represent positive (negative) SLP anomalies and thick solid green contour is zero SLP value in (a) and (c).

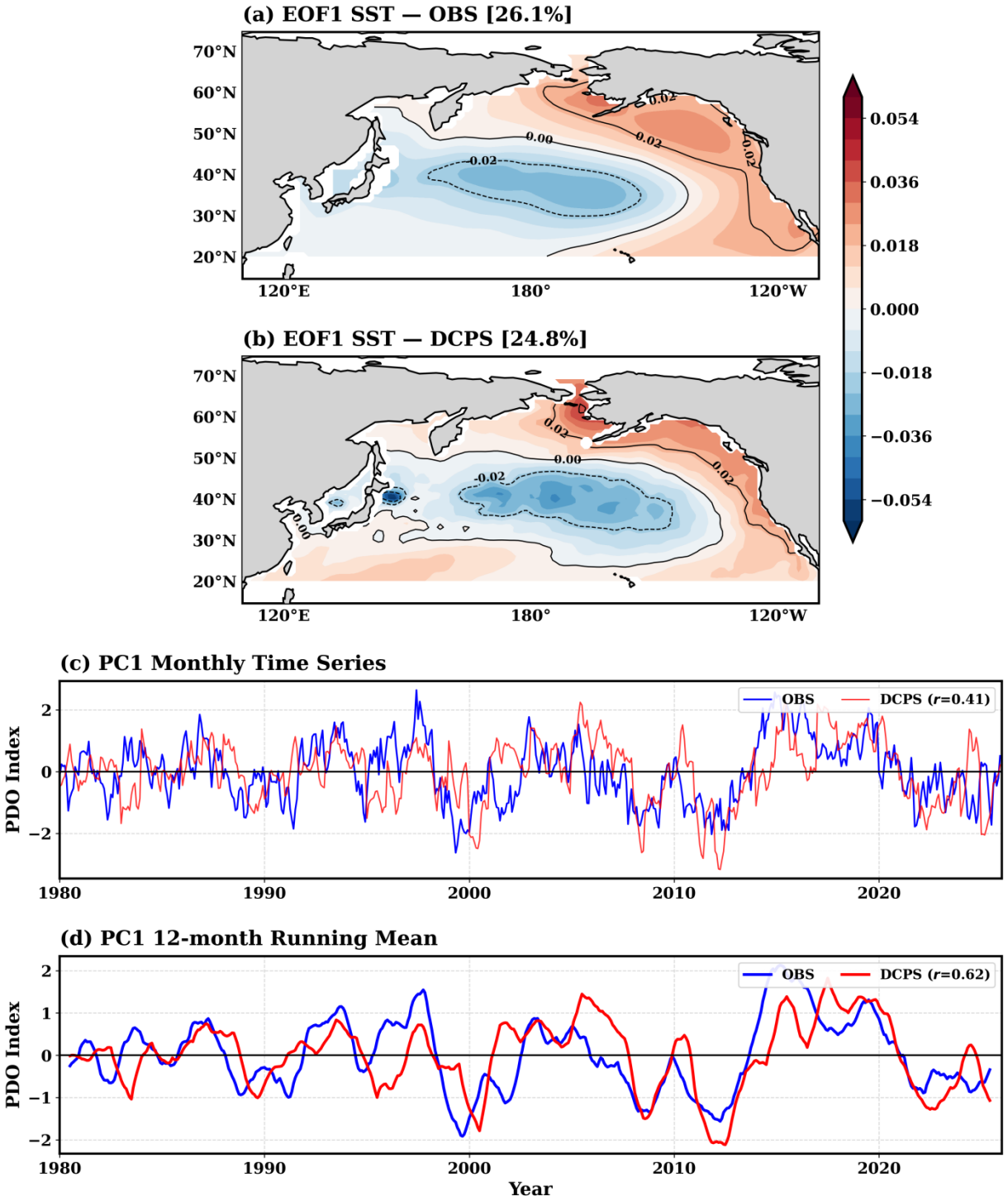


Figure 19. Spatial patterns and temporal evolution of PDO for LY1. (a) Observed (ERSSTv5) first EOF pattern, explaining 26.1% of the variance, and (b) IITM-DCPS hindcasts, explaining 24.8% of the variance, based on North Pacific SST anomalies. Dashed and solid contours represent negative and positive loadings, respectively. (c) Monthly PC1 time series for observations (blue) and IITM-DCPS (red), with a correlation coefficient of r = 0.41. (d) Corresponding 12-month running-mean PC1 time series, with r = 0.62.

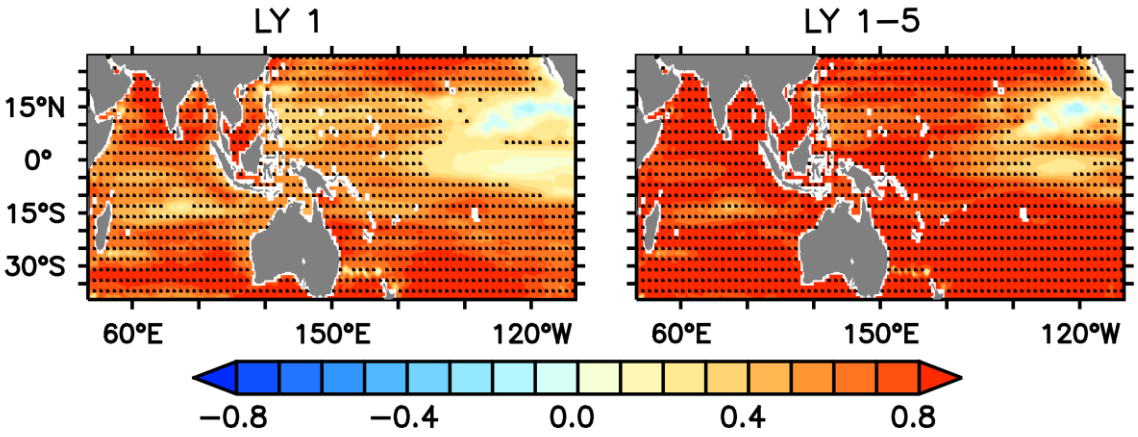


Figure 20. Spatial ACC of annual mean SLA of IITM-DCPS with respect to ORAS5, at LY1 and LY1-5

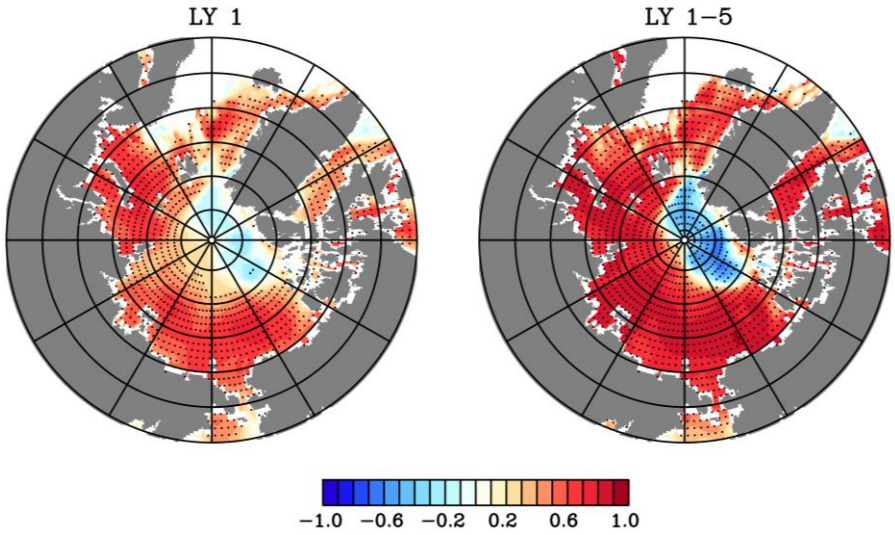


Figure 21. ACC of annual mean SIC anomalies of IITM-DCPS over Arctic with respect to ORAS5, at LY 1 and LY 1-5.